UNIVERSITÀ DEGLI STUDI DI PADOVA

DEPARTMENT OF CIVIL, ENVIRONMENTAL AND ARCHITECTURAL ENGINEERING

MASTER THESIS IN WATER AND GEOLOGICAL RISK ENGINEERING

IN-SITU AND REMOTE SENSING CHARACTERIZATION OF SALINITY-AFFECTED AGRICULTURAL AREAS IN THE PO RIVER DELTA

SUPERVISOR

Marco Marani

CO-SUPERVISOR

Tegan Blount

MASTER CANDIDATE

Oğuzhan Şahin

STUDENT ID

2070752

ACADEMIC YEAR

2023/2024

ACKNOWLEDGEMENTS

I would like to express my deepest gratitude to my thesis supervisor, Professor Marco Marani, for believing in me, trusting in my abilities, and agreeing to guide me through this thesis. His unwavering support and patience from the beginning to the end of this journey have been invaluable.

I would like to express my deepest gratitude to Tegan Blount for her invaluable advice on remote sensing and data acquisition and processing, which significantly contributed to the success of this research.

My sincere thanks also go to Dr. Alice Puppin for her expert guidance and support during the lab work and to Prof. Andrea D'Alpaos for generously providing access to the laboratory at the Geosciences Department.

I am deeply indebted to Ing. Rodolfo Laurenti, Director of Consorzio di Bonifica Adige-Po, for his assistance in identifying and facilitating access to the study site, without which this research would not have been possible.

My heartfelt thanks go to my father, mother, older brother, and sister, whom I have not seen since arriving in Italy in September 2022, for their support and belief in my success.

Rovigo, Italy ... 2024

Oğuzhan Şahin

ABSTRACT

Salinity-induced land degradation in agricultural areas poses significant challenges to sustainable farming practices, particularly in regions like the Po River Delta, an area where agricultural land lies several meters below mean sea level. This thesis explores the characterization of salinity-affected agricultural areas through a combination of in-situ and remote sensing techniques. By employing drone-based remote sensing, remote sensing technologies, and laboratory analysis, the study tackles the complexities of soil salinization and vegetation stress in the Po Delta region, in an area near Porto Tolle where soil salinization has been documented in previous years. Utilizing multi-spectral images from the Planet data provider, this work maps vegetation stress responses to salinity using the NDVI index. Fieldwork involved the collection and analysis of 13 soil samples from the surface and from a depth of about 45-155 cm along a transect to explore if traces of past salinization events are identifiable. The integration of soil salinity data with drone and satellite multispectral data facilitated a comprehensive mapping study of salinity-affected agricultural land, highlighting the utility of remote sensing in monitoring land degradation processes in relation to the resolution of the data. By correlating remote sensing data with laboratory results, this thesis contributes to define the accuracy and repeatability of remote-sensing observations to derive quantitative information on the spatial and temporal distribution of soil salinization, with implications for decision making in the management of reclaimed agricultural land in the Po River Delta.

Key words: On-site sensing, Remote sensing, Soil salinization, Vegetation stress, Po River Delta.

CONTENTS

LIST OF FIGURES

LIST OF TABLES

CHAPTER 1: INTRODUCTION

Soil salinization is one of the most important global environmental problems, especially in arid and semiarid regions (Chen et al., 2014). Information regarding the extent and magnitude of soil salinity is essential for the planning and implementation of effective soil reclamation programs (Abdelfattah et al., 2009). Accurate information about the extent, magnitude, and spatial distribution of salinity may, in fact, be used to develop sustainable strategies for the development of agricultural resources (Bannari et al., 2008).

Soil salinization is a progressive process of soil degradation involving the accumulation of water-soluble salts at and near the soil surface (Nawar et al., 2015 & Oosterbaan, 2020). These salts can include sulphates (SO4), carbonates (CO3), and chlorides (Cl) in concentrations that may give saline soils a characteristic whitish surface crust when dry. Salts naturally occur in soils, but when their concentration becomes too high, it can negatively impact plant growth and soil fertility.

Salinization can be caused by natural processes such as mineral weathering as well as by artificial processes such as excessive and improper irrigation (Oosterbaan, 2020). On the other hand, water dynamics in the soil also influence salinity, particularly in areas where saline groundwater is very close to or at the ground surface, and evaporation exceeds precipitation (Dehaan and Taylor, 2002). This case for example occurs in reclaimed land near the coast during periods of drought, in which irrigation is insufficient to keep sea water from percolating into the fields, often facilitated by the presence of highly conductive ancient river reaches buried beneath the surface.

A significant example of salinization processes leading to high impacts on agricultural activities are observed in Italy's Po River Delta. Agricultural irrigation, industrial usage, power generation, and other human activities can lead to increased water consumption throughout the Po River Basin, especially during drought periods. This heightened demand for water may reduce the discharge of fresh water in the river (Luo et al., 2023) and lead to sea water moving up the Delta several tens of kilometres. Consequently, saltwater intrusion into the surrounding lowlands may occur, causing salts to rise and accumulate in the top soil layer. This process adversely affects soil fertility, reduces productivity, and may permanently degrade coastal agricultural areas (Guerra-Chanis et al., 2019).

Several techniques exist for measuring soil salinity, which can be conducted in both field and laboratory settings, as well as, indirectly, remote sensing methods. The choice of technique often depends on factors such as the desired scale, required accuracy, and the resources at hand. Each approach offers unique advantages, allowing for flexibility in assessing soil salinity across different environments and conditions.

Soil salinity can be expressed by electrical conductivity (EC), which may be associated with corresponding impacts on the crops. Soil with EC > 4 dS/m (decisiemens per meter) at 25 °C will be harmful to crops and will affect plant growth (Morshed et al., 2016).

Laboratory methods for the measurement of soil salinity are based on the determination of total dissolved salts (TDS) or of the electrical conductivity (EC) of soil water extracts, (Rayment and Higginson, 1992).

Remotely sensed data and Geoinformatics caused a revolution in research related to agriculture, land, water, marine and geomorphology (Abdelfattah et al., 2008). Remote Sensing and GIS techniques can be an excellent tool for mapping saline and waterlogged soils (De Dapper et al., 1997). Soil salinity maps can be produced using several remote sensing techniques that are effective in measuring soil salinity levels. The mapping and monitoring of salinity involves two critical steps: first, identifying areas where salts concentrate, and second, detecting the temporal and spatial changes in this phenomenon. The success of these efforts largely depends on the unique distribution patterns of salinity at the soil surface and within the soil layer, as well as the capability of remote sensing tools to identify salt (Zinck, 2001).

The objective of this thesis is to investigate the characterization of salinity-affected agricultural areas using a blend of in-situ observations and remote sensing techniques. Specifically, the study employed drone-based remote sensing, remote sensing technologies, and comprehensive laboratory analyses to address the intricacies of soil salinization and its subsequent impact on vegetation stress in the Po Delta region, particularly near Porto Tolle, where soil salinization has been previously documented. This research also maps the potential effects of soil salinity on vegetation stress by utilizing satellite-based NDVI (Normalized Difference Vegetation Index), providing valuable insights into the challenges faced by agricultural practices in this region.

In this context, the thesis questions are: What is the impact of soil salinity on vegetation stress in agricultural areas of the Po River Delta, and how can we effectively map salinity-affected regions using satellite and drone-based remote sensing technologies in conjunction with supporting laboratory data?

In line with the search for answers to these questions, multispectral data with acquired on the study area from the years 2017 to 2023 were downloaded from the Planet Scope Scene satellite data provider. Additionally, multispectral imagery of the study area were captured using a drone, and the data were processed with Agisoft Metashape Pro software to create an orthomosaic map. This approach is aimed at producing a comprehensive mapping of plant stress in salinity-affected agricultural fields by effectively integrating satellite and drone-derived multispectral data, supplemented with laboratory data.

CHAPTER 2: LITERATURE REVIEW

2.1. Definition and Importance of Salt-affected soil

Salt-affected soils consist of saline and sodic soils, occur in all continents and under almost all climatic conditions, but their distribution is relatively more extensive in the arid and semi-arid regions compared to the humid regions. Soil salinization and sodification are major soil degradation processes threatening ecosystem and are recognized as being among the most important problems at a global level for agricultural production, food security and sustainability in arid and semi-arid regions.

Fig. 1 Agricultural field affected by soil degradation: (a) Soil salinization and (b) Soil sodification, as documented by Food and Agriculture Organization (Food and Agricultural Organization, 2024).

Soil salinity and sodicity are two related but distinct problems that can affect the quality of soil and its suitability for agriculture. Soil sodicity specifically pertains to excessive sodium levels, while soil salinity refers to the concentration of soluble salts in the soil.

Sodicity refers to the presence of excess sodium (Na+) ions in the soil. While sodium is an essential nutrient for plants, high levels of sodium can cause soil structural problems and reduce its ability to support plant growth. Sodicity is often associated with soil salinity, but it specifically refers to the dominance of sodium ions over other cations like calcium (Ca2+) and magnesium (Mg2+).

Soil salinity refers to the concentration of soluble salts present in the soil, including compounds such as sulphates (SO4), carbonates (CO3), and chlorides (Cl). Soil salinization is also the process by which these water-soluble salts accumulate in the soil (Wang et al., 2023). High salinity levels can adversely affect plant growth by reducing the soil's ability to retain moisture and causing ion toxicity. Over time, salinization can lead to reduced agricultural productivity and soil degradation.

2.2. Causes of Soil Salinity

Soil salinity is a widespread problem that affects agricultural productivity and environmental health. While human activities like irrigation and poor drainage often contribute to soil salinity, natural factors also play a significant role in its development. Understanding natural and anthropogenic causes are crucial for developing effective management strategies.

2.2.1. Natural Factors

One of the primary natural sources of soil salinity is the weathering of parent rocks and minerals. As rocks break down over time, they release salts into the soil. This process is especially significant in arid and semi-arid regions where rainfall is insufficient to leach salts away from the soil surface (Yadav and Singh, 2015).

Coastal areas are particularly susceptible to soil salinity due to seawater intrusion. This occurs when seawater seeps into groundwater or surface water systems, leading to increased salt concentrations in the soil. Factors such as rising sea levels and reduced freshwater inflow can exacerbate this issue (Peterson, 2001).

Natural salt deposits can also contribute to soil salinity. These deposits are often found in areas that were once covered by ancient seas or lakes. As these bodies of water evaporated, they left behind layers of salt that can be mobilized into the soil through wind or water erosion (Khan and Duke, 2018). In arid and semi-arid regions, high evaporation rates can concentrate salts in the soil surface. When water evaporates, it leaves behind any dissolved salts, increasing the salinity of the upper soil layers. This process is especially pronounced in areas with shallow groundwater, where capillary action draws saline water to the surface (Yadav and Singh, 2015).

Salts can also be introduced into the soil through atmospheric deposition. This includes the deposition of airborne sea salts carried inland by wind, as well as the deposition of salts from volcanic eruptions or dust storms. These processes can increase the salinity of soils far from direct sources of salt. Additionally, geological uplift can expose salt-rich strata that were previously buried beneath the Earth's surface. Over time, these exposed layers can contribute to soil salinity as they undergo weathering and erosion (Watson, 2005).

2.2.2. Anthropogenic Factors

Soil salinity is a major environmental issue significantly influenced by human activities. Anthropogenic factors often exacerbate the natural processes that lead to increased salt concentrations in the soil, resulting in negative impacts on agricultural productivity and ecosystem health.

One of the primary anthropogenic causes of soil salinity is the improper use of irrigation. Excessive irrigation can lead to waterlogging, which raises the water table and brings dissolved salts to the soil surface through capillary action (Shrivastava and Kumar, 2015). This process is especially problematic in regions where drainage systems are inadequate or absent, allowing salts to accumulate over time. The use of saline water for irrigation is another

significant factor contributing to soil salinity. In areas where fresh water is scarce, farmers often rely on brackish groundwater or saline surface water for irrigation, which introduces large quantities of salts into the soil (Rengasamy, 2006). Over time, the repeated application of saline water can lead to severe salinity issues.

Land clearing and deforestation can also contribute to soil salinity. Removing vegetation reduces the uptake of water by plants, which can increase the amount of water that percolates into the soil, raising the water table. This process can mobilize salts that were previously stored in the soil profile and bring them to the surface (George et al., 2012). Industrial and urban activities contribute to soil salinity through the release of saline effluents and wastewater. Industries such as mining and manufacturing often discharge saline water into surrounding environments, increasing the salt content of soils and water bodies (Qadir et al., 2007). Urbanization also leads to increased impervious surfaces, which reduce natural infiltration and exacerbate runoff and salinity issues.

The excessive use of fertilizers and soil amendments can also lead to soil salinity. Many fertilizers contain salts, and their over-application can increase the salt concentration in the soil. Additionally, the use of certain soil amendments, such as gypsum, in inappropriate amounts or without proper management can contribute to salinity problems (Munns and Tester, 2008).

2.3. Impacts of Salinity on Crop Yield and Quality

Soil salinity is a critical factor affecting agricultural productivity, with significant implications for crop yield and quality. When soluble salts in the soil reach high concentrations, they create an unfavourable environment for plant growth. This salinity stress disrupts the ability of plants to absorb water and essential nutrients, leading to reduced crop performance (Ahmed et al., 2024)

Highly tolerant crops can endure salt concentrations in the saturation extract of up to 10 g/L, which corresponds to the liquid phase that interacts directly with plant roots. The moderately tolerant crops can withstand salt concentration up to 5 g/l. Sensitive group of crops begins to suffer salinity effects at about 2.5 g/l.

The tolerance levels of various crops to salt concentration are presented in Table 1 (Brouwer et al., Food and Agriculture Organization, 1985). Additionally, the agronomic classification of soil salinity based on the electrical conductivity of the saturation extract (EC_e) is also given in Table 2 (Brown et al., 1954).

Table 1

Classification of crops based on their tolerance to salt concentration (Brouwer et al., Food and Agriculture Organization, 1985)

Highly tolerant	Moderately tolerant	Sensitive
Date palm	Wheat	Red clover
Barley	Tomato	Peas
Sugar beet	Oats	Beans
Cotton	Alfalfa	Sugarcane
Asparagus	Grape	Soybean
Spinach	Rice	Pear
	Maize	Apple
	Flax	Orange
	Potatoes	Prune
	Carrot	Plum
	Onion	Almond
	Cucumber	Apricot
	Pomegranate	Peach
	Fig	
	Olive	

Table 2

Agronomic classification of soil salinity based on electrical conductivity of the saturation extract (EC_e) (Brown et al., 1954)

Classification	EC_e (dS/m)	Crop yield
Non-saline soils	0-2	Not affected
Slightly saline soils	2-4	Sensitive crop affected
Saline soils	4-8	Many crops affected
Strongly saline soils	8-16	Only tolerant crops possible
Extremely saline soils	>16	A few very tolerant crops possible

High salinity levels create osmotic stress, which makes it difficult for plant roots to take up water from the soil. This water stress stunts plant growth, leading to decreased crop yields (Atta et al., 2023 & Flowers and Yeo, 1995). In addition, the excess salts interfere with the uptake of key nutrients such as potassium, calcium, and magnesium, causing nutrient imbalances that further weakens plants and reduces their productivity (Flowers and Yeo, 1995).

Specific ions, like sodium (Na+) and chloride (Cl-), can accumulate to toxic levels in plant tissues, resulting in leaf burn, necrosis, and diminished photosynthetic activity (Atta et al., 2023 & Flowers and Yeo, 1995). These symptoms of ion toxicity further contribute to lower yields. Additionally, salinity can affect seed germination, hindering plant establishment and reducing the overall crop density, which limits yield potential (Atta et al., 2023).

Soil salinity also impacts crop quality in several ways. The nutritional content of crops can be altered, affecting the levels of proteins, carbohydrates, and essential vitamins and minerals (Atta et al., 2023). This change can diminish the nutritional value of harvested produce. The crops grown in saline conditions may have reduced storage potential and a shorter shelf life due to altered biochemical and physiological properties (Ahmed et al., 2024 & Flowers and Yeo, 1995).

2.4. In-Situ and Laboratory Measurement Techniques for Soil Salinity

Monitoring soil salinity in situ is crucial for managing soil health and agricultural productivity. Several techniques have been developed to measure soil salinity directly in the field, providing real-time data for effective management decisions. Employing suitable sampling methods and conducting laboratory analysis can enhance the accuracy of these measurements, offering valuable insights into salinity levels in agricultural fields.

2.4.1. Electrical Conductivity (EC) Sensors:

Electrical conductivity sensors are widely used for measuring soil salinity in situ. These sensors determine the soil ability to conduct electrical current, which is directly related to the concentration of dissolved salts, even though the relation between EC and dissolved ions also depends on the specific ions present. EC sensors can be inserted into the soil to provide continuous or periodic measurements, allowing for real-time monitoring of salinity levels (Corwin and Lesch, 2005).

2.4.2. Time Domain Reflectometry (TDR):

Time domain reflectometry is a method that uses electromagnetic waves to measure the dielectric constant of the soil. Since the dielectric constant is affected by the soil moisture content and salinity, TDR can be used to estimate soil salinity indirectly. TDR probes are inserted into the soil, and the travel time of the electromagnetic wave is used to calculate salinity levels (Dalton et al., 1984).

2.4.3. Electromagnetic Induction (EMI):

Electromagnetic induction is a non-invasive technique used to map soil salinity over large areas. EMI instruments generate a magnetic field that induces a secondary field in the soil, which is measured to estimate soil salinity. This method is useful for identifying spatial variability in salinity across fields and landscapes without disturbing the soil (McNeill, 1980).

2.4.4. Resistivity Sensors:

Resistivity sensors measure the resistance of soil to the flow of electrical current. Since saline soils have lower resistance due to the presence of ions, these sensors can provide an estimate of soil salinity. Resistivity measurements can be made using electrodes placed at different depths in the soil to assess salinity profiles (Samouelian et al., 2005).

2.4.5. Optical Sensors:

Optical sensors, such as near-infrared (NIR) sensors, are used to estimate soil salinity by measuring the absorption and reflection of light at the visible (400-700 nm) and near-infrared (700-2500 nm) wavelengths range. These sensors can be mounted on equipment like drones or tractors to provide rapid assessments of salinity across large areas (Sudduth et al., 2005).

2.4.6. Sampling and Laboratory Analysis

Soil salinity may be determined in the laboratory by measuring the electrical conductivity of soil water extracts, soluble ion concentrations of soil water, mass of total dissolved solids (TDS), or total dissolved ions (TDI) (Hardie and Doyle, 2012).

Electrical conductivity (EC) measures how well a medium, such as soil or water, can conduct an electric current. This property is crucial for understanding how substances conduct electricity, which can be important in various scientific and practical applications (Rhoades et al., 1999).

Historically, electrical conductivity was reported using units like micro-mhos per centimeter (μmho/cm) or milli-mhos per centimeter (mmho/cm) (Hardie and Doyle, 2012). These units represent the reciprocal of electrical resistance and are used to describe how easily electric current can flow through a medium. However, these units have been largely replaced by the International System of Units (SI) for greater consistency and standardization.

In the SI system, the unit used to measure electrical conductivity is the Siemens (S). Electrical conductivity is expressed as the reciprocal of electrical resistance, which is measured in ohms. Therefore, one Siemens is equal to one reciprocal ohm (Rhoades et al., 1999). For practical purposes, especially in fields like agriculture and environmental science, electrical conductivity is often reported in deci-Siemens per meter (dS/m), which one dS/m is equivalent to 1 mmhos/cm (millimhos per centimetre) or 1,000 μS/cm (microSeimens per centimetre) (Hardie and Doyle, 2012). Conversions between units are presented in Table 3.

Table 3

Conversion (multiply by) of electrical conductivity units and approximate salt concentrations (Hardie and Doyle, 2012)

From/to	dS/m	mS/m	μS/m	mS/cm	μS/cm
dS/m	1	100	100,000	1	1,000
mS/m	0.01	1	1,000	0.01	10
μS/m	0.00001	0.001	1	0.00001	0.01
mS/cm	1	100	100,000	1	1,000
μS/cm	0.001	0.1	100	0.001	1
TDI mg/L	0.0015	0.15	150	0.0015	1.5
Meq/L	0.1	10	10,000	0.1	100

However, soil salinity is most commonly measured as electrical conductivity (EC) of a 1:5 soil:distilled water suspension following one hour of mixing as shown in the salinity classes

in electrical conductivity ($EC_{1:5}$) in Table 4 (Rayment and Higginson, 1992). Electrical conductivity is a surrogate measure of salinity in which the salt content of a soil water suspension is determined based on its ability to conduct electricity between two metal electrodes. The more salt in the soil suspension, the more current is conducted between the two electrodes, resulting in higher EC values. Electrical conductivity values also depend on the temperature. Measurements must thus be corrected for this effect, usually with reference to a standard temperature of 25°C (Rayment and Higginson, 1992).

Table 4

Salinity classes in electrical conductivity as $EC_{1:5}$ for different soil textures (Rayment and Higginson, 1992)

Salinity class	$EC_{1:5}$ range for sands (dS/m)	$EC_{1:5}$ range for loams (dS/m)	$EC_{1:5}$ range for clays (dS/m)
Non-saline	0–0.14	0–0.18	0–0.25
Slightly saline	0.15–0.28	0.19–0.36	0.26–0.50
Moderately saline	0.29–0.57	0.37–0.72	0.51–1.00
Highly saline	0.58–1.14	0.73–1.45	1.01–2.00
Severely saline	1.15–2.28	1.46–2.90	2.01–4.00
Extremely saline	>2.28	>2.90	>4.00

2.5. Remote Sensing Techniques for Salinity Assessment

The analysis of saline areas utilizing multispectral imagery data from remote sensing technology relies on visual interpretation methods, including natural and false colour composites (see Table 5) by combinations of the band reflectance, along with the calculation of various indices (see Table 6) to generate maps based on the evaluation of vegetation stress resulting from soil salinity.

Table 5

Colour composites employed for assessing vegetation stress related to soil salinity, utilizing various band combinations.

Colour composite	Band combination
Natural	R – G – B
Colour infrared (vegetation)	SWIR2 – SWIR1 – R
Agriculture	SWIR1 – NIR – B
Healthy vegetation	NIR – SWIR1 – B
Vegetation analysis	SWIR1 – NIR – R
Vegetation and Presence health	NIR – R – G

* B, blue band; G, green band; R, red band; RE, red-edge band; NIR, near-infrared band; SWIR1-2, short-wave infrared band

Table 6

Equations of vegetation and spectral salinity indices used in soil salinity assessment (Xie et al., 2018 & Gad et al., 2022)

Index	Formula	Reference
Normalized difference vegetation index (NDVI)	(NIR – R) / (NIR + R)	Rouse, Jr. et al., 1974
Normalized difference vegetation index $(NDVI)_{Red\text{-}edge}$	(NIR – RE) / (NIR + RE)	Gitelson et al., 1994
Normalized difference salinity index (NDSI)	(R – NIR) / (R + NIR)	Khan et al., 2001
Salinity Index 1 (SI_1)	$(G \times R)^{1/2}$	Douaoui et al., 2006
Salinity Index 2 (SI_2)	$(B \times R)^{1/2}$	Khan et al., 2001
Salinity Index 3 (SI_3)	(B – R) / (B + R)	Bannari et al., 2008
Salinity Index 4 (SI_4)	(NIR / R)	Major et al., 1990
Salinity Index 5 (SI_5)	(R x NIR) / G	Abbas and Khan, 2007
Salinity Index 6 (SI_6)	(B x R) / G	Abbas and Khan 2007

* B, blue band; G, green band; R, red band; RE, red-edge band; NIR, near-infrared band

2.5.1. Satellite-Based Remote Sensing

Satellite-based remote sensing is a vital tool in assessing soil and water salinity across various landscapes, offering a comprehensive view that allows for large-scale monitoring and management of salinity issues in agricultural and coastal regions. The primary advantage of satellite remote sensing lies in its ability to cover extensive areas with consistent and repeatable observations, which are crucial for understanding salinity dynamics over time (Khan, et al., 2005).

Numerous studies have utilized various types of sensors, including thermal, multispectral, hyperspectral, and microwave, to quantify salt content in soils (Hu et al., 2019; Guo et al., 2019). Each of these sensors offers distinct spectral, spatial, radiometric, and temporal resolution characteristics, significantly influencing the scope and relevance of the research (Allbed et al., 2013). Table 7, as presented by Sahbeni et al. (2023), summarizes the most commonly used sensors for detecting soil salinization and their respective characteristics.

Table 7

An overview of commonly used sensors for salinization assessment and their characteristics, including spatial, spectral, and temporal resolutions, acquisition cost, and applicable mapping scale (Sahbeni et al., 2023).

Sensor	Spatial Resolution (m)	Spectral resolution	Temporal Resolution (Day)	Acquisition Cost	Applicable Mapping Scale
MODIS	250-500	36	1	Free	Regional/Global
Landsat	30-120	8-11	16	Free	Local/Regional
Sentinel 2	10-60	13	5	Free	Local/Regional
ASTER	15-90	14	16	Low	Local/Regional
IKONOS	4	5	3	High	Local
Planet Scope	3	8	1	Low/Medium	Local/Pixel plot
Worldview	<5	9	1	Low/Medium	Local/Pixel plot
Sentinel 1	5		6	Free	Local/Regional
RADAR	5			High	Local/Regional
Hyperspectral	1	>200		High	Pixel-plot
Unmanned Aerial Vehicle (UAV)	~2.5 cm	>200		Medium/High	Pixel-plot

The sensors listed in Table 7 have proven effective in identifying patterns across various spatiotemporal scales, with spatial resolutions ranging from a few centimetres to several hundred meters and revisit intervals between one day and two weeks (Zhu et al., 2017). However, the effective implementation of remote sensing tools for assessing salinization is contingent upon data availability and the scale of the investigation (Sahbeni et al., 2023). Consequently, both the technical specifications of the sensor and the availability of data are critical factors in selecting an appropriate remote sensing system for salinization assessment.

Multispectral and hyperspectral imaging are one of the key technologies used in satellite-based salinity assessment. Satellites equipped with multispectral sensors capture data in several specific wavelengths across the electromagnetic spectrum. This is critical for identifying the spectral signatures associated with salt-affected areas and assessing vegetation health, which indirectly indicates soil salinity levels. Hyperspectral sensors capture data across hundreds of narrow spectral bands, providing detailed information about soil and vegetation conditions. This allows for precise identification of salinity levels and the differentiation between various types of salts (Metternicht and Zinck, 2003).

Thermal infrared imaging is another important technology used in satellite-based salinity assessment. Thermal infrared sensors on satellites measure surface temperature variations, which can be used to infer soil moisture content. Since saline soils typically exhibit distinct thermal properties due to evaporation rates, thermal imaging is valuable for indirect salinity assessment (Verma, et al., 1994).

Microwave remote sensing, particularly Synthetic Aperture Radar (SAR), is used to detect soil moisture levels. SAR is capable of penetrating cloud cover and can be used to monitor soil moisture changes, which are often correlated with salinity levels (Zribi et al., 2011).

Satellite remote sensing is widely used in agriculture to monitor soil salinity levels, providing essential data for precision agriculture. By identifying saline areas, farmers can implement targeted soil management practices to mitigate salinity impacts and improve crop yields (Bastiaanssen, et al., 2000). In coastal and inland water bodies, satellites monitor salinity to help manage water resources, assess the impacts of salinity on aquatic ecosystems, and plan land use (Rao and Dekker, 2014). Additionally, satellite-based salinity assessments inform environmental research and land management strategies by providing insights into the effects of salinity on biodiversity and ecosystem health (Dehaan and Taylor, 2003).

The advantages of using satellites for salinity assessment include large-scale coverage, temporal consistency, and cost-effectiveness. Satellites can cover extensive areas, providing consistent and repeatable observations crucial for monitoring salinity dynamics over time (Khan et al., 2005). The regular revisit times of satellites allow for consistent temporal monitoring, which is essential for tracking changes in salinity levels (Verma et al., 1994). While the initial investment in satellite data may be high, the ability to monitor large areas over time makes it cost-effective compared to ground-based methods (Zribi et al., 2011).

However, there are also challenges and limitations associated with using satellites for salinity assessment. The spatial resolution of some satellite sensors may not be sufficient for detailed salinity assessments at smaller scales (Allbed and Kumar, 2013). Analysing large volumes of satellite data requires significant computational power and expertise (Bastiaanssen et al., 2000). Atmospheric conditions can affect the accuracy of satellite data, particularly in optical and thermal infrared sensors (Metternicht and Zinck, 2003).

Overall, satellite-based remote sensing plays a critical role in salinity assessment by providing comprehensive and repeatable observations over large areas. This capability supports sustainable land and water management practices by enabling the effective monitoring and management of salinity issues (Khan et al., 2005).

2.5.2. Drone Technologies

Drone technology has become an integral tool in remote sensing, particularly for environmental assessments such as salinity assessment in agricultural and coastal areas. The use of drones in remote sensing offers numerous advantages, including high-resolution data collection, flexibility in operation, and cost-effectiveness compared to traditional methods like satellite imagery and manned aircraft (Mulla, 2013).

One of the key technologies used in drone-based salinity assessment is multispectral and hyperspectral imaging. Drones equipped with multispectral cameras capture data in multiple specific wavelengths across the electromagnetic spectrum. This data is essential for assessing vegetation health and soil conditions by identifying spectral signatures associated with salt-affected areas (Li & Yang, 2018). Hyperspectral sensors provide even finer spectral resolution

by capturing data across hundreds of narrow spectral bands, which allows for more precise identification of soil salinity levels and differentiation between salt types (Mulla, 2013).

Thermal imaging is another important technology used in drone-based salinity assessment. Thermal cameras mounted on drones can detect variations in soil moisture content. Saline soils often exhibit distinct thermal properties due to differences in moisture evaporation rates, which enable indirect salinity assessment (Peralta and Costa, 2013). Additionally, Light Detection and Ranging (LIDAR) technology is used to create detailed topographic maps. These maps help identify areas prone to waterlogging and salinity due to elevation changes and poor drainage (Shrestha and Farshad, 2009).

Advanced data processing techniques, including machine learning algorithms, are employed to analyse the complex data collected by drones. These algorithms can improve the accuracy of salinity maps by correlating spectral data with ground-truth salinity measurements (Li and Yang, 2018).

Drone technology has several applications in salinity assessment. In agriculture, drones are used to monitor soil salinity levels, providing crucial data for precision agriculture. By identifying saline areas, farmers can implement targeted soil management practices to improve crop yields (Ghassemi et al., 1995). In coastal areas, drones assist in mapping salinity levels, which can affect ecosystems and human activities. Accurate salinity mapping aids in managing land use and mitigating the impacts of saltwater intrusion (Shrestha and Farshad, 2009). Additionally, researchers use drone-collected data to study the effects of salinity on biodiversity and soil health, informing conservation efforts and land management strategies (Li and Yang, 2018).

Drones can fly at low altitudes, capturing high-resolution images that are crucial for detailed salinity assessment (Mulla, 2013). They can be deployed quickly and easily in remote or hard-to-reach areas, allowing for frequent and timely data collection (Zhang and Kovacs, 2012). Compared to satellite imagery and manned aircraft, drones offer a more affordable solution for large-scale environmental monitoring (Ghassemi et al., 1995).

However, there are also challenges and limitations associated with using drones for salinity assessment. Regulatory issues can limit their deployment in certain areas (Zhang and Kovacs, 2012). Additionally, the large volumes of data generated by drones require significant processing power and expertise to analyse effectively (Li & Yang, 2018). Weather dependence is another limitation, as adverse weather conditions can affect drone flights and impact data collection (Mulla, 2013).

2.6. Case Studies of Salinity Monitoring in the Po River Delta

2.6.1. Saltwater intrusion in the Po River Delta (Italy) during drought conditions: Analysing its spatio-temporal evolution and potential impact on agriculture

The article conducted by Luo et al. (2023) explores the complex dynamics of saltwater intrusion in the Po River Delta, emphasizing both the spatio-temporal variations and the associated agricultural impacts resulting from drought conditions. With this study, the authors

identify and delineate areas in the Po Delta region that are particularly affected by salinity. This research provides valuable insights into the multifaceted nature of saltwater intrusion, underscoring its significant implications for local agriculture. Additionally, it highlights the urgent need for advanced methodologies to effectively predict and manage future risks associated with this environmental challenge.

2.6.1.1. Key Findings

2.6.1.1.1. Saltwater Intrusion Dynamics

The research emphasizes that saltwater intrusion is a highly nonlinear and time-varying phenomenon, influenced by a multitude of factors, including climate change, tidal oscillations, and human activities. Notably, the year 2006 marked the most severe instance of saltwater intrusion, while preliminary data suggests that 2022 may surpass it in severity.

2.6.1.1.2. Agricultural Impact

A significant negative correlation was found by authors between salinity levels and the Normalized Difference Vegetation Index (NDVI), suggesting that increased salinity adversely affects agricultural greening and productivity.

2.6.1.1.3. Spatial and Temporal Variability:

The research demonstrated significant spatial and temporal variability in saltwater intrusion, with some areas being more vulnerable than others due to changes in river discharge and tidal influences

2.6.1.2. Methodology

The study assesses the impact of saltwater intrusion on agricultural greening by analyzing the Normalized Difference Vegetation Index (NDVI), a widely used indicator of plant health and greening, while not the primary objective of the study. NDVI data were collected from Landsat 5 satellite imagery over the Po River Delta during periods of saltwater intrusion. The researchers examined how variations in salinity levels influenced NDVI values, which reflect the vegetation's photosynthetic activity and overall health.

To understand the relationship between salinity and crop performance, the study compared NDVI trends with salinity levels recorded along the river. The analysis involved correlating changes in NDVI with shifts in salinity, highlighting how increased salt concentration negatively impacted crop growth, as evidenced by lower NDVI values. Spatial analysis techniques were used to map these relationships across the delta, providing a detailed view of how salinity intrusion during drought conditions affected different agricultural areas.

2.6.1.2.1. Indicator of Agricultural Greening (NDVI):

The Normalized Difference Vegetation Index (NDVI) was used as an indicator of agricultural greening, allowing researchers to assess the health of vegetation in relation to salinity levels.

NDVI provides a quantitative measure of vegetation cover and health, which is crucial for understanding the impact of environmental stressors like saltwater intrusion.

2.6.1.2.2. Impact of Salinity on Crops and Implications on NDVI:

The research demonstrated that increased salinity levels have a detrimental impact on crop health, as reflected in decreased NDVI values. The correlation between salinity and NDVI underscores the importance of monitoring salinity as a key factor affecting agricultural productivity in the region.

2.6.1.3. Results

2.6.1.3.1. Historical Analysis of Saltwater Intrusion

The analysis of data from 2006 to 2022 reveals significant saltwater intrusion events, with 2006 and 2022 identified as particularly severe years. Fig. 2 presents a location map of the Po River Delta, detailing the study conducted in areas affected by saltwater intrusion during the droughts of 2006 and 2022.

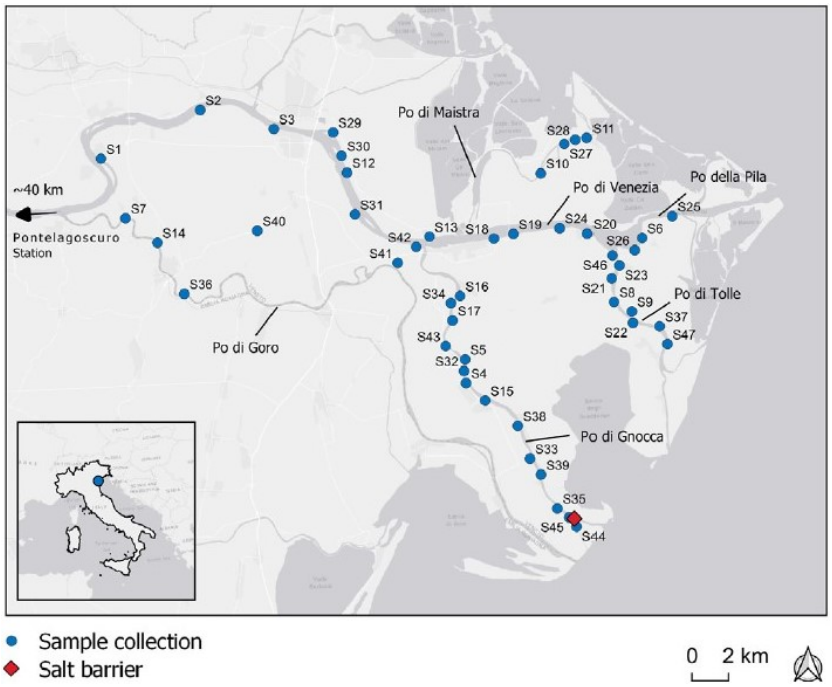

Fig. 2 Po River Delta area in northern Italy, along the Adriatic coast (lower box). The main map details the location of water sampling points used for salinity measurement are shown. It also shows the locations of the Po Gnocca Valle salt barrier (in red). The black arrow indicates that Pontelagoscuro station is about 40 km from the indicated point to the west (Luo et al., 2023)

Salinity levels recorded in the Po River Delta over this period are illustrated in Fig. 3.

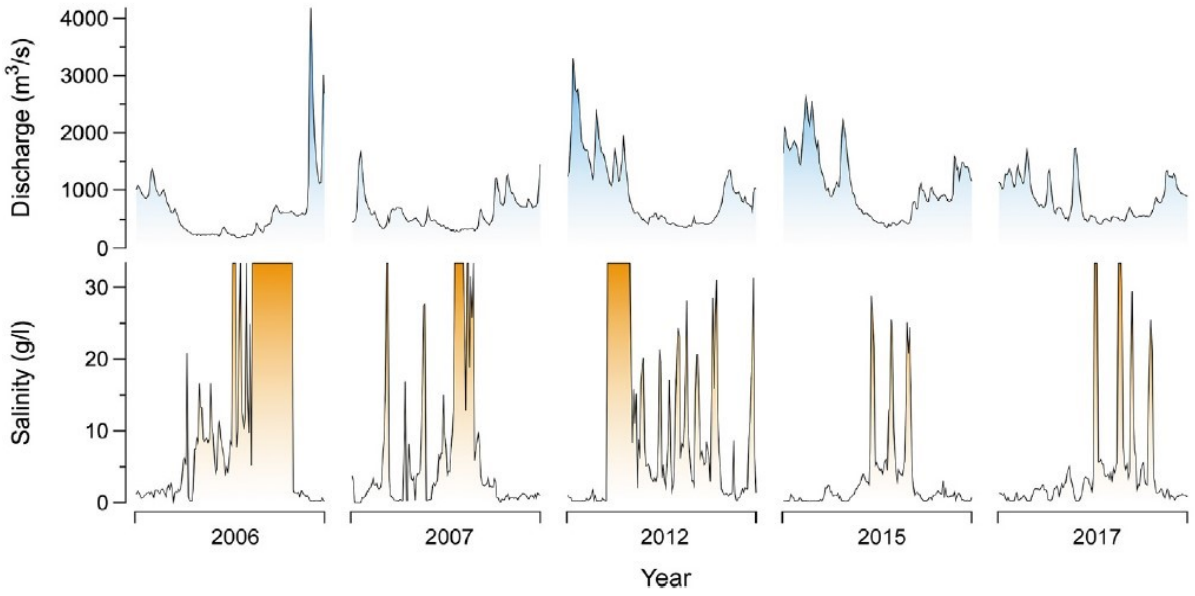

Fig 3 Variations of discharge and salinity during the drought periods; the salinity is measured at the saltbarrier of Po Gnocca Valle permanent station and the discharge is measured at Pontelagoscuro (Luo et al., 2023).

As depicted in Fig. 3, the year 2007 had average and minimum discharge values of 611 m³/s and 287 m³/s, respectively, with an average salinity of 6.5 g/l. In 2012, the average and minimum discharge values increased to 976 m³/s and 363 m³/s, respectively, accompanied by an average salinity of 10.1 g/l. For 2015, the average and minimum discharge values were 1,090 m³/s and 363 m³/s, respectively, while the average salinity was recorded at 3.1 g/l. In 2017, the average and minimum discharge values were 832 m³/s and 424 m³/s, respectively, with an average salinity of 4.4 g/l. The salinity data for 2022 is not included in Figure 3 as it is still being processed by the researchers. Based on the salinity and discharge data, the researchers concluded that 2006 was the most critical year for saltwater intrusion (Luo et al., 2023).

2.6.1.3.2. Temporal and Spatial Variability

The findings showcase considerable spatio-temporal variability in saltwater intrusion, indicating that certain areas are more susceptible due to fluctuations in river discharge and tidal influences (refers to Fig. 4).

The maps in Fig. 4 visually demonstrate the spatial distribution of salinity, emphasizing the regions that experienced the highest levels of intrusion in July and August 2006 and clearly shows the dynamics of interpolated salinity data along the rivers over time. In the last week of July in 2006, with the decrease in discharge (see Fig. 3), saltwater intrusion extended almost the entire delta system (Fig. 4(a)). The maximum saltwater intruded into the delta up to 12.5, 9.2, 11.1, 20.4, and 22.3 km upstream of the river mouths of the Maistra, Pila, Tolle, Gnocca, and Goro branches, respectively. Salinity values greater than 30 g/l are found up to 6 km from the river mouth in the Maistra and Tolle branches. This saltwater intrusion occurred four days after the Po Delta reached the historical minimum discharge record (189.24 m^3/s) (during the summer of 2022, however, the 2006 record was broken by a new value of 104 m^3/s, Tarolli et al., 2023). About one month later, saltwater intrusion eased gradually with the increase of

discharge (Fig. 4(b)). The phenomenon of large salinity in the lower reaches of the delta area is closely related to the near shore currents of the Adriatic Sea and the estuarine dynamics.

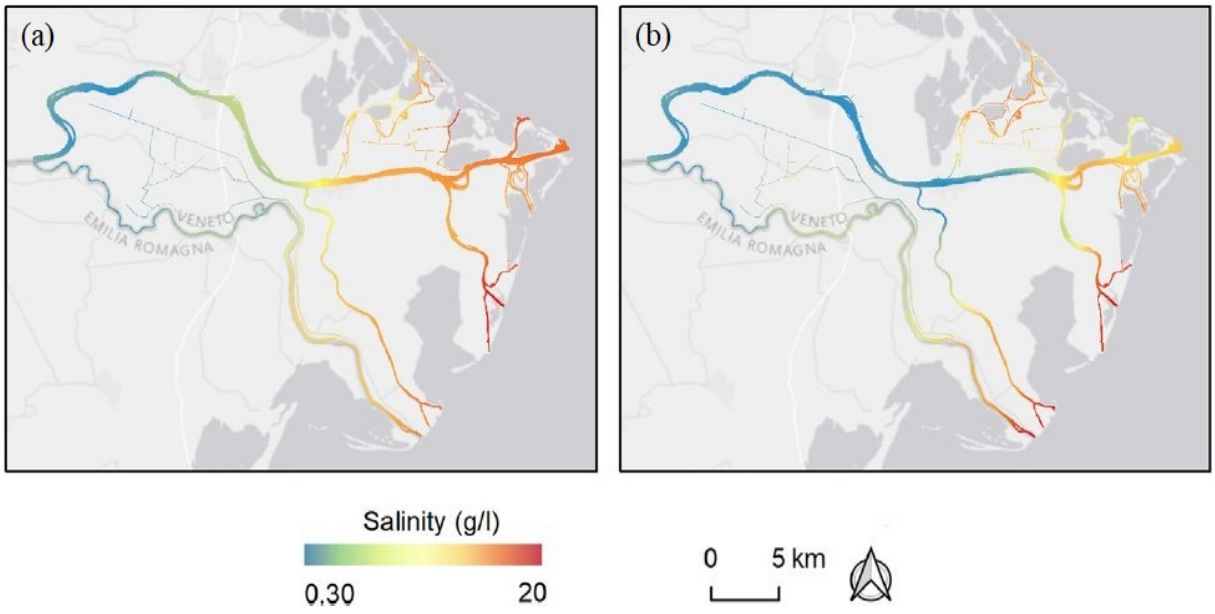

Fig. 4 Spatial-temporal evolution of saltwater intrusion in Po River delta in 2006; (a) and (b) represent July and August, respectively (Luo et al, 2023)

Researchers also observed a negative correlation between salinity values and the average NDVI with increasing distance from the sea. This trend is consistent with the higher salinity measurements typically observed in river water closer to the sea than in inland areas (see Fig. 4).

2.6.1.3.3. Impact on Agriculture

The study highlights the detrimental effects of saltwater intrusion on agricultural health, as areas with elevated salinity levels experience diminished vegetation health, as evidenced by NDVI measurements. This underscores the potential risks to agricultural productivity in the region during periods of heightened saltwater intrusion.

2.6.2. Saltwater Intrusion and Climate Change Impact on Coastal Agriculture

The research conducted by Tarolli et al. (2023) provides a comprehensive analysis of the challenges posed by climate change and saltwater intrusion on agricultural systems in coastal regions. Focusing on two vulnerable areas; the Po River Delta in Italy and the Mekong Delta in Vietnam, the study highlights how these regions are increasingly threatened by the adverse effects of saltwater intrusion. Climate change factors such as rising sea levels, diminished river flows, and prolonged droughts exacerbate this vulnerability. The authors emphasize the necessity of implementing sustainable management practices and mitigation strategies to safeguard agricultural productivity in these critical areas.

2.6.2.1. Key Findings

2.6.2.1.1. Impact of Saltwater Intrusion

The study reveals that saltwater intrusion, intensified by climate change, poses a significant threat to agricultural productivity in coastal regions. In the Po River Delta, frequent droughts coupled with reduced river discharge have enabled saltwater to infiltrate deeper inland, adversely affecting crop growth and soil health (see Fig. 5). Similarly, the Mekong Delta faces substantial challenges due to upstream dam constructions and land subsidence, resulting in increased soil salinity and diminished agricultural viability.

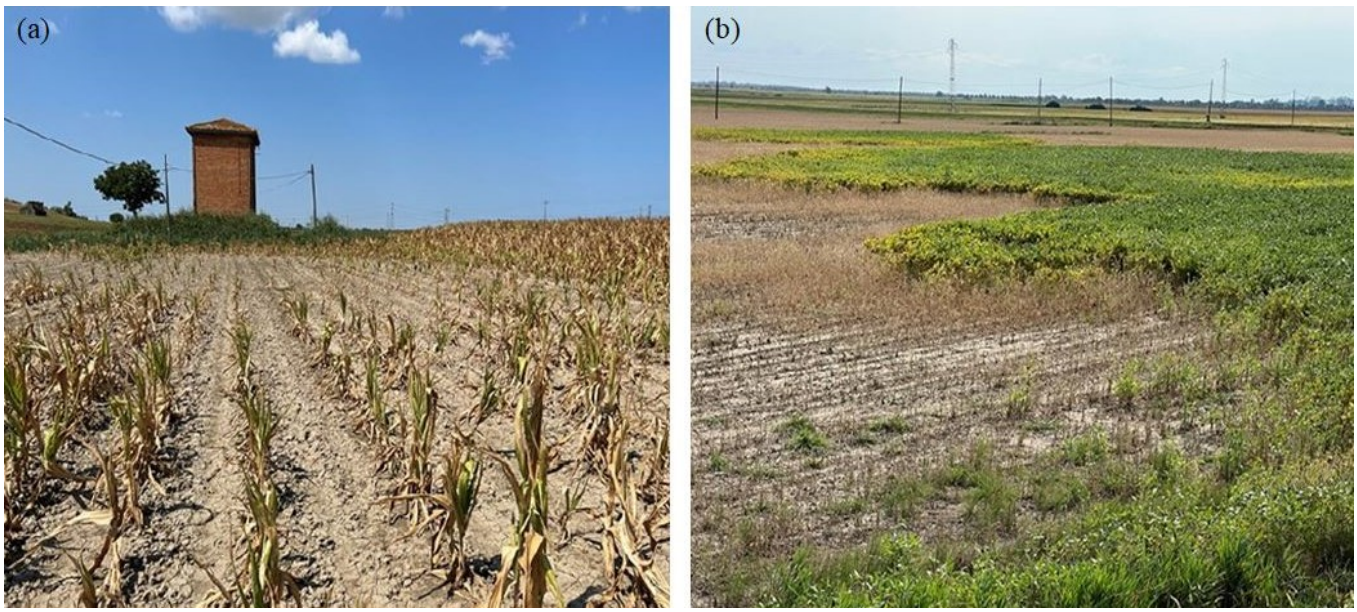

Fig. 5 Some remarkable effects of saltwater intrusion on crops in the Po River Delta delta during summer 2022; (a) and (b) represent maize and soybean fields, respectively (Tarolli et al., 2023) (photos by Paolo Tarolli).

2.6.2.1.2. Comparative Analysis

The paper provides a comparative analysis of the droughts in the Po River Delta in 2006 and 2022, illustrating a troubling trend of escalating saltwater intrusion severity linked to extended periods of low river flow and insufficient precipitation as shown in Fig. 6. This trend raises concerns about the future agricultural productivity of the region if current environmental conditions persist or deteriorate.

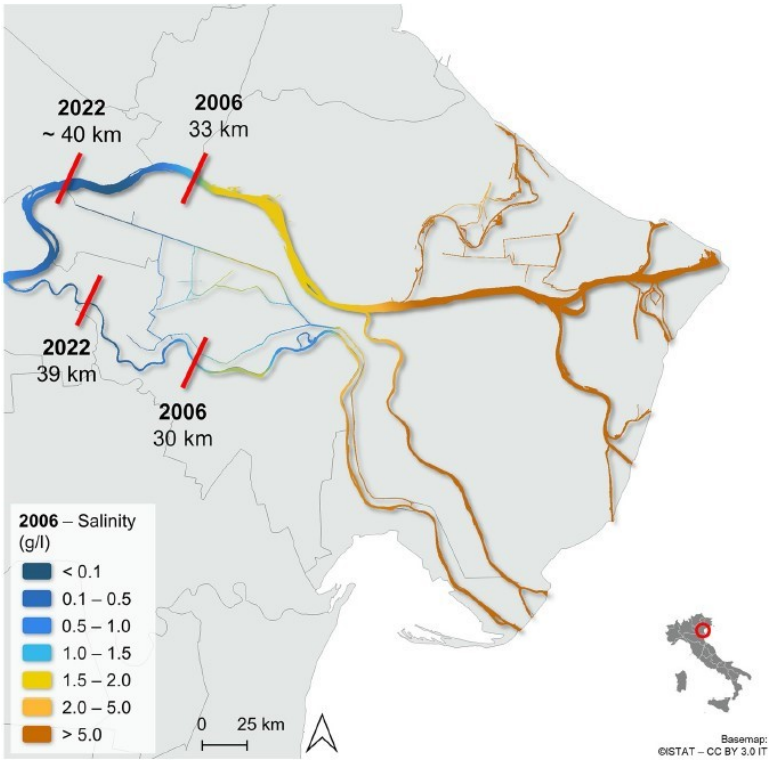

Fig 6 Saltwater intrusion in the Po River Delta during the two major droughts of summer 2006 and 2022. The limits indicating where water salinity exceeded the critical threshold for agriculture (2 g/l) are shown in red, along with the relative distance from the sea. Also displayed are the boundaries of the 2022 drought event, which was even more severe than the 2006 event (Tarolli et al., 2023)

Fig. 6 provides an overview of the 2006 drought and compares it to the 2022 drought. An important difference to underline between the two droughts is the long duration of the 2022 phenomenon in terms of exceptionally low river flow and concomitant absence of precipitation (2.5 months of persistent crisis). Freshwater from the Po River is a primary resource for the entire agricultural landscape of the delta, which is used for irrigation through a capillary canal network. When water salinity exceeds the critical threshold, it becomes complex and sometimes impossible to comply with irrigation scheduling, aggravating the severe water shortage. The consequences are dramatic for agricultural production and can manifest as soil fertility deterioration, vegetation loss, and micro desertification of large field portions (Tarolli et al., 2023).

2.6.2.1.3. Mitigation Strategies

The research proposes several mitigation strategies, including the construction of mobile barriers to obstruct saltwater intrusion during low river discharge periods, the promotion of rainwater harvesting to secure fresh water during droughts, and the adaptation of agricultural practices to incorporate salt-tolerant crop varieties.

2.6.2.1.4. Future Challenges

The paper cautions against the increasing frequency of extreme weather events, which could further compound saltwater intrusion issues. It stresses the importance of a collaborative

approach that involves local communities, scientists, and policymakers to devise and implement effective long-term solutions.

2.6.2.2. Methodology

2.6.2.2.1. Data Collection and Analysis

The study employs a robust methodology that includes the collection and analysis of data pertaining to river discharge, soil salinity, and agricultural productivity spanning several decades. This data serves as a foundation for identifying trends and forecasting future impacts.

2.6.2.3. Results

2.6.2.3.1. Increased Saltwater Intrusion

The findings indicate a marked increase in saltwater intrusion in both the Po and Mekong Deltas, with more frequent and severe occurrences in recent years. This escalation has resulted in considerable challenges for agriculture, including soil salinization, decreased crop yields, and the degradation of arable land.

2.7. Future Directions in Salinity Research

Soil salinization monitoring studies are rapidly advancing, driven by continuous technological innovations and an increasing diversity of methodologies, including field studies, laboratory analyses, and the satellite and drone-based remote sensing.

Despite these advancements, each method comes with inherent limitations, highlighting the challenges researchers encounter when monitoring and mapping areas affected by soil salinity. For instance, while sensors such as Electrical Conductivity (EC), Time Domain Reflectometry (TDR), and Electromagnetic Induction (EMI) offer practical solutions for salinity detection in field studies, their high costs often restrict their use to a limited number of researchers and consequently narrow the scope of salinity research. Laboratory analyses of saline soil samples also play a crucial role in salinity measurement. However, potential errors arising from human factors in the preparation and measurement of soil/water extracts can significantly impact the accuracy of salinity determinations.

The advent of satellite and drone-based remote sensing has revolutionized the detection and mapping of salinity, particularly in large areas facing salinity challenges. Nonetheless, the diversity in satellite and sensor capabilities, along with their varying levels of accessibility, can hinder small-scale researchers. For example, while free and accessible satellites like Sentinel and Landsat provide data at resolutions of 10 to 60 meters and 30 to 120 meters, respectively, these resolutions may not suffice for effective salinity detection in smaller study areas. Moreover, the high costs associated with advanced multi-spectral imagery from sensors such as high-resolution RADAR and UAVs further limit research opportunities.

To address these gaps, a comprehensive approach that integrates field, laboratory, and remote sensing technologies is essential for enhancing salinity detection and mapping in agricultural

landscapes. By comparing data gathered through various methodologies for a selected salinity-affected agricultural area, researchers can better address the limitations inherent in each method. This triangulation of data will not only improve the accuracy and reliability of salinity assessments but also contribute to a more holistic understanding of salinization processes.

In summary, acknowledging the existing limitations in salinity research opens up valuable avenues for future investigation. By fostering collaboration across diverse methodologies and tackling accessibility challenges, we can enhance our comprehension of the impact of soil salinity on agricultural land. This approach will also facilitate more effective mapping of salinity-affected areas, ultimately contributing to better management practices and mitigation strategies.

2.8. Conclusion

This literature review has synthesized key findings on the challenges and management of salt-affected soils, particularly in arid and semi-arid regions. The review explored the fundamental distinctions between soil salinity and sodicity, along with their natural and anthropogenic causes, which include irrigation practices, poor drainage, and climate change. The adverse effects of soil salinity on agricultural productivity, soil structure, and ecosystem health were also highlighted, emphasizing the urgent need for effective monitoring and management strategies. The adverse effects of soil salinity on agricultural productivity, soil structure, and ecosystem health are well-documented, with salinity stress leading to reduced water and nutrient uptake, ion toxicity, and ultimately lower crop yield and quality.

The review emphasizes the urgent need for effective monitoring and management strategies, underscoring the importance of accurate and timely detection of salinity levels. Various methodologies for monitoring soil salinity, such as in-situ techniques and remote sensing, have been discussed. Remote sensing, in particular, is highlighted as a powerful tool for large-scale monitoring, enabling the identification of salinity trends over time and across vast agricultural landscapes.

Additionally, the socio-economic implications of soil salinity are considered, noting that the livelihoods of farmers and rural communities are significantly affected by the degradation of agricultural lands due to salinity. The review underscores the need for policies that support sustainable land management and provide resources for farmers to implement effective salinity control measures. Furthermore, it identifies varying degrees of salt tolerance among different crops, providing a basis for informed crop selection and management practices in saline environments.

In conclusion, the literature offers a comprehensive understanding of the causes, impacts, and measurement techniques of soil salinity, forming the foundation for developing effective management strategies to mitigate the adverse effects of soil salinization. This knowledge is essential for sustaining agricultural productivity and enhancing soil health in vulnerable regions, thereby informing future research and practical interventions aimed at combating soil salinity.

CHAPTER 3: MATERIALS AND METHODOLOGY

3.1 Study area

To identify the study area, engineers from the Consorzio Adige-Po in Rovigo assisted in locating a local farmer who had expressed concerns about salinization in his field. During the field survey, it was decided to select this farmer's field as the study area, as both citizens and stakeholders consistently highlighted the salinization issue affecting the land.

The study area consists of an agricultural field characterized by light clay soil, where soybeans are grown (Glycine max; planted in April - May and harvested from September (Luo et al., 2023)). Light clay contains a significant proportion of clay particles, though it is not as dense as heavy clay soils. It is easier to work with than heavy clay, while still retaining a relatively high capacity for holding water (Gibbs, 2000).

This field is situated in the eastern part of Rovigo Province, within the Commune of Porto Tolle. It is situated within latitudes (44°54'54.94"N) and longitudes (12°26'46.50"E) with total area approximately 46,000 m^2. The elevation of the field is about 3 m below sea level. The climate is warm, muggy and low cloudy in summer with an average temperature of about 24 °C, too cold and partly cloudy in winter with an average temperature about of 5 °C, and average annual rainfall of 46 mm/year (Weather Spark, 2024).

Positioned along the Po della Tolle branch of the Po River as shown in Fig. 8, the field experiences soil salinization impacting vegetation cover. Thus, it presents a suitable test area of change detection utilizing remote sensing data.

Fig. 7 The soybean field in Porto Tolle, Italy, exhibiting the detrimental effects of soil salinization (photos by O. Şahin, 29 August 2024).

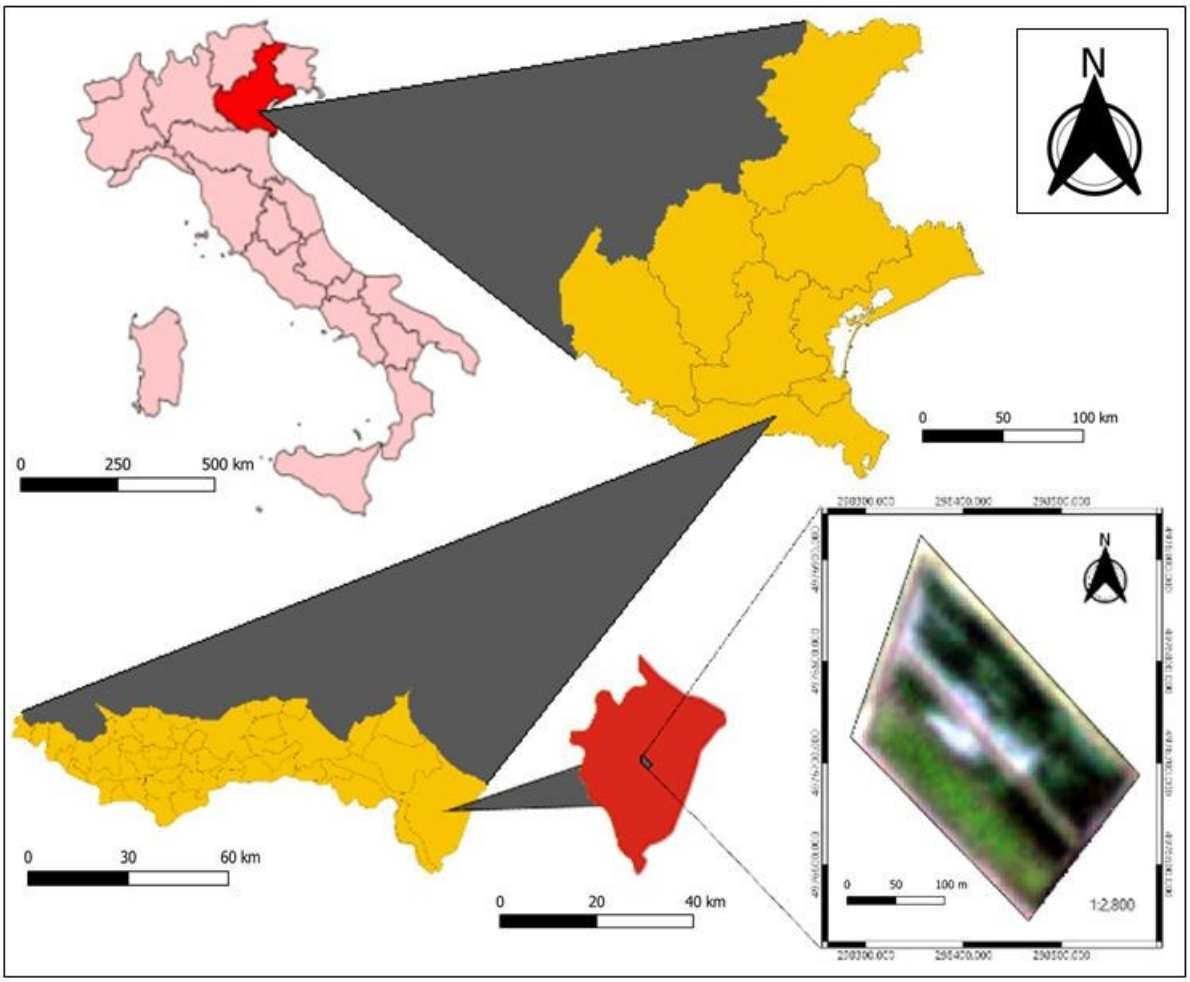

Fig. 8 Natural colour composite (RGB: 321) of the Planet Scope imagery taken on August 18, 2021, along with a positional map of the study area. The map of Italy is shown in the upper right corner (pink), while the map of the Veneto region is located in the upper left corner (yellow). The Rovigo province map is positioned in the lower left corner (yellow), and the map of the Porto Tolle commune is displayed in the lower center (red).

3.2 Determining the study area coordinates using GPS technology

The location of the study area was determined by marking 50 distinct points within the soybean field and accurately recording the coordinates of each point using a GPS device under the supervision of Dr. Tegan Blount. These GPS coordinates were then processed as a CSV file using the 'Add Layer' and 'Add Delimited Text Layer' functions in QGIS (Quantum Geographic Information System) software. From within the 50 points, points 2, 3, 4, and 50 were selected for soil sampling, as depicted in Fig. 9. The objective of this study was to investigate whether evidence of historical salinization events could be detected by analysing soil salinity, which is quantified in the laboratory through the measurement of electrical conductivity (EC) in soil/water extracts.

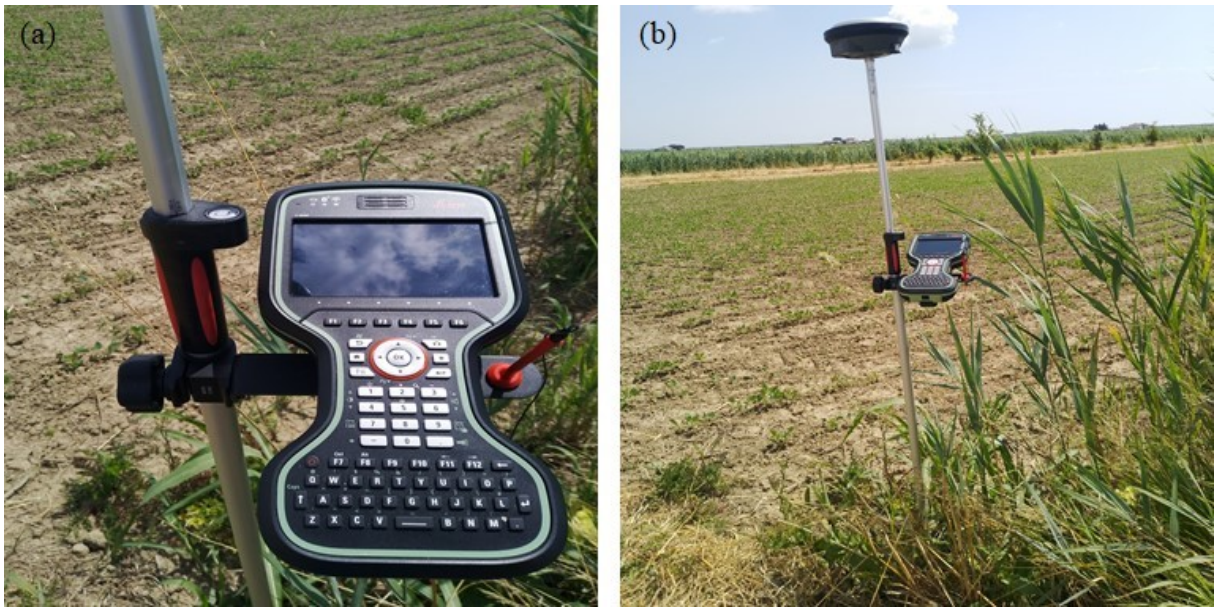

Fig. 9 The process of determining the coordinates of soil sample points using GPS technology: (a) The GPS device utilized for marking sampling locations, and (b) The initial setup of the GPS device to establish the reference point.

3.3 Soil sample collection for soil salinity level measurement

Soil sampling was conducted on Monday 10 June, 2024 at the edge of the Tolle branch in the Po River Delta. The sampling process involved taking samples along a vertical transect that traversed the agricultural land in the southwest-northeast direction as shown in Fig. 10.

Fig. 10 Sampling point locations using QGIS, projected to WGS84 and UTM coordinate system on Google Satellite imagery

A total of 13 soil samples were collected from four distinct locations (points 2, 3, 4, and 50) within the study area and samples collected were securely packed in plastic bags without any additives as illustrated in Fig. 11. Surface samples were gathered from the top layer (0-10 cm) using a shovel, while deeper samples were extracted at varying depths between 42.2 and 155 cm using a soil core auger as shown in Fig. 12. The variation in sampling depths as shown in Table 8 was necessary due to the differing consistency of the soil at each sample point, which posed challenges when trying to reach soil layers deeper than tilling depth.

Table 8

Distribution of soil depths of samples collected at sample points 2, 3, 4 and 50.

Quantity of sample	1	2	3	4
Sampling point	**Depth (cm)**			
2	Soil surface	44.2-56.0	80.0-85.0	145.0-155.0
3	Soil surface	45.0-55.0	90.0-100.0	-
4	Soil surface	45.0-55.0	70.0-80.0	-
50	Soil surface	45.0-50.0	63.0-73.0	-

***** The depth of soil samples collected from the soil surface varies between 0-10 cm.

Fig. 11 Packaging of soil samples collected from sampling locations 2, 3, 4, and 50. A total of 13 soil samples were gathered, each placed in a labelled plastic bag corresponding to its respective sampling point. The samples were carefully handled prior to being stored in a cool oven for preservation, ensuring the integrity and quality of the soil for laboratory analysis. (photo by O. Şahin).

Fig 12 Collecting soil samples using a core auger from designated sampling points in the soybean field, within the scope of the field study: (a) photo by Prof. Marco Marani, and (b, c, d, e, f, g, and h) photos by Dr. Tegan Blount

3.4. Laboratory analysis of saline soil samples collected

Laboratory procedures were carried out under the guidance of Dr. Alice Puppin, in the Geoscience laboratory of the Department of the Geosciences at the University of Padova, Italy on Thursday 25 July and Monday 29 July, 2024. The procedures lasted a total of two days, and all tools and equipment used to measure the salinity of soil/water extracts are listed in Table A1 in the Appendix.

The process is based on determining the salinity levels in the laboratory by measuring the electrical conductivity (EC) of soil water extracts, expressed in µS/cm (microseimens per centimetre). This method adheres to the $EC_{1:5}$ Soil/Water extract technique as outlined in M. Hardie and R.B. Doyle (2012). Additionally, a sensitivity analysis of the grain size using the sample exhibiting the highest salinity was conducted to assess the sensitivity of the obtained salinity value to grain size. The $EC_{1:5}$ readings were converted to actual soil salinity (EC_e), which indicates the potential impact of soil salinity on plant growth. This conversion is achieved by applying a factor that corresponds to the texture of the soil sample (see Table 9, Gibbs, 2000), as described in Equation (1):

$$EC_e = EC_{1:5} \times MP \quad (1)$$

Where EC_e is actual soil salinity (dS/m), $EC_{1:5}$ is electrical conductivity value of soil/water extracts for one-to-five (dS/m), and MP is multiplication factor, which equals 8.6 for light clay.

Table 9
$EC_{1:5}$ to EC_e Conversion Factors (Gibbs, 2000)

Soil Texture	Multiplication Factor
Sands	17
Sandy Loams	13.8
Loams	9.5
Clay Loams & Light Clays	8.6
Medium & Heavy Clays	7

* These factors are calibrated for southern NSW (AU) soils by S.Gibbs (2000)

3.4.1. $EC_{1:5}$ (EC one-to-five) Soil/Water Extract

The method consists of the direct (instrumental) determination of electrical conductivity in aqueous soil extracts at a 1:5 soil-to-water ratio:

1. Approximately 50 g of each soil sample was weighed in separately plastic beakers using a precision scale and then placed in a cool oven (Memmert) to dry at 60 °C and 50% ventilation for 24 hours (see Fig. 13).

2. The dried soil samples were crushed with a mortar-a-pestle and rolling pin and then passed through a 2 mm sieve to remove impurities such as plant material and stones (see Fig. 14).

3. To prepare a one-to-five soil/water extract using plastic tubes and a spoon, 25 mL of deionized water was added to every 5 g of dried soil (see Fig. 15).

4. The prepared soil/water extracts were mechanically shaken horizontally for 30 minutes at 25 °C using an orbital shaker to dissolve soluble salts. Subsequently, the soil was allowed to settle for approximately 15 minutes (see Fig. 16)

5. The Conductometer (WTW-Cond 340i) was calibrated according to the WTW's instructions (see Table 1A).

6. The conductivity cell of the conductometer was immersed in the supernatant and gently moved up and down without disturbing the settled soil. When the system stabilized, the reading was taken with the cell stationary (see Fig. 17). To prevent erratic readings in salinity measurements between samples, the conductivity cell was rinsed with deionized water, and excess water was removed. EC measurements were completed approximately 3-4 hours after all aqueous supernatants were obtained.

7. $EC_{1:5}$ values in µS/cm (microSiemens per cm) for each aqueous supernatant were recorded at 25 °C on an air-dry basis. The results (dS/m) were multiplied by the conversion factor (8.6 for Clay Loams and Light Clays, as referenced in Table 9) based on soil texture to obtain soil salinity (EC_e), indicating the potential impact of soil salinity on plant growth.

Fig. 13 Drying step of soil samples collected from the field: (a) Labelling each soil sample by depth using beakers; (b) Weighing 50 g of each soil sample; (c) Placing the prepared samples in a cool oven for drying (Note: The soil samples visible on the lower shelves of the cool oven belong to another researcher); (d) Setting the cool oven to 60 °C and initiating the drying process (photos by O. Şahin).

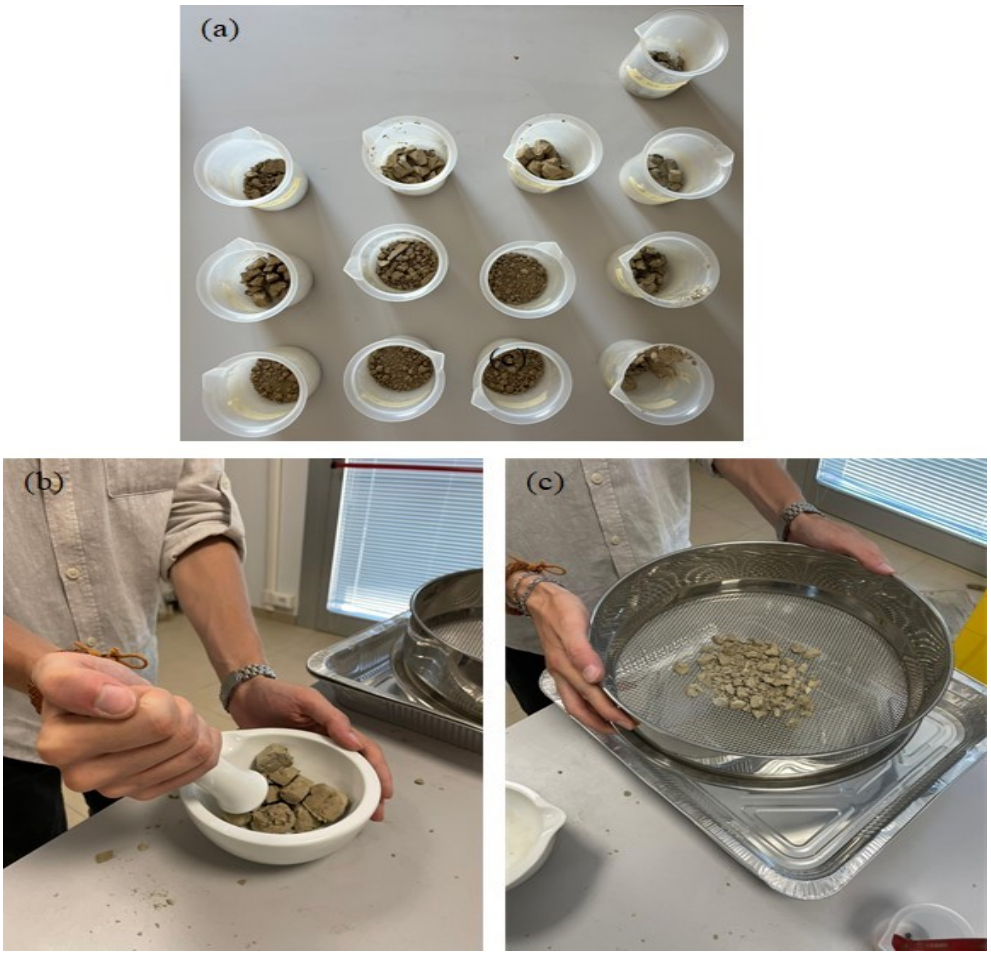

Fig. 14 Steps involved in grain size reduction and sieving of dried samples: (a) Dried soil samples after 24 hours; (b) Crushing the dried soil sample with a mortar and pestle to reduce grain size; (c) Sieving the soil sample through a 2 mm sieve to remove impurities such as plant material and stones (photos by A. Puppin and O. Şahin).

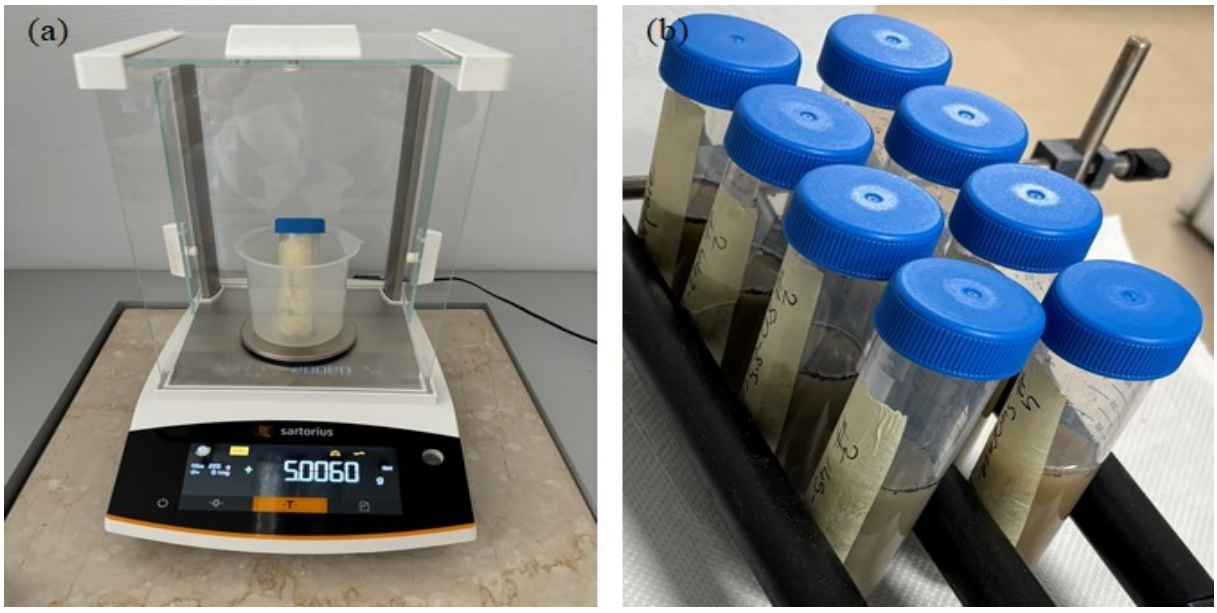

Fig. 15 Steps involved in the preparation of a 1:5 soil/water extract: (a) Weighing 5 g of the dried and sieved soil sample after accounting for the weight of the beaker and tube on a precision scale; (b) Mixing the 5 g of soil sample in plastic tubes with the addition of 25 mL of deionised water (photos by O. Şahin).

Fig. 16 Shaking and resting process of the prepared soil/water extracts: (a) Shaking the extracts horizontally for 30 minutes using an orbital shaker; (b) Allowing the shaken extracts to rest for 15 minutes (photos by O. Şahin).

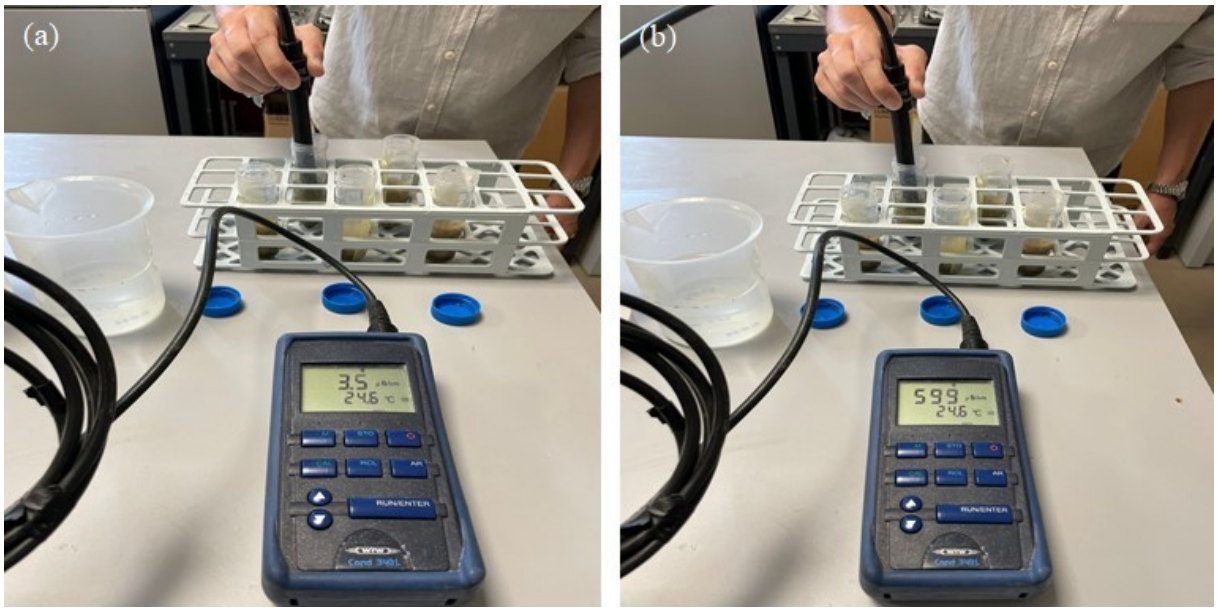

Fig. 17 Step of the measuring soil salinity levels in the extracts using a conductometer: (a) Starting to measure salinity level using the conductometer, and (b) Waiting for the electrical conductivity value (µS/cm) to stabilize on the conductometer before recording the readings (photos by A. Puppin).

3.4.2. Sensitivity Analysis for grain size

The relationship between soil salinity and soil particle size is consistent with the relationship between soil metal content and soil particle size (Zhao et al., 2016). Research by Al-Rajahi et al. (1996) and Ljung et al. (2006) indicates that metal concentrations in soil tend to increase as particle size decreases. This phenomenon occurs because finer particles possess a larger specific surface area, which enables them to retain greater quantities of metals (Acosta et al., 2009).

To evaluate the sensitivity of the salinity values to grain size, a sensitivity analysis was conducted using the sample exhibiting the highest salinity. The highest recorded salinity level was 1158 µS/cm, which belongs to sample point 4 from a depth of 70-80 cm (refers to Table 7).

In this analysis, both finer and coarser grain sizes were obtained using 0.5 mm and 4 mm sieves, as illustrated in Fig. 18.

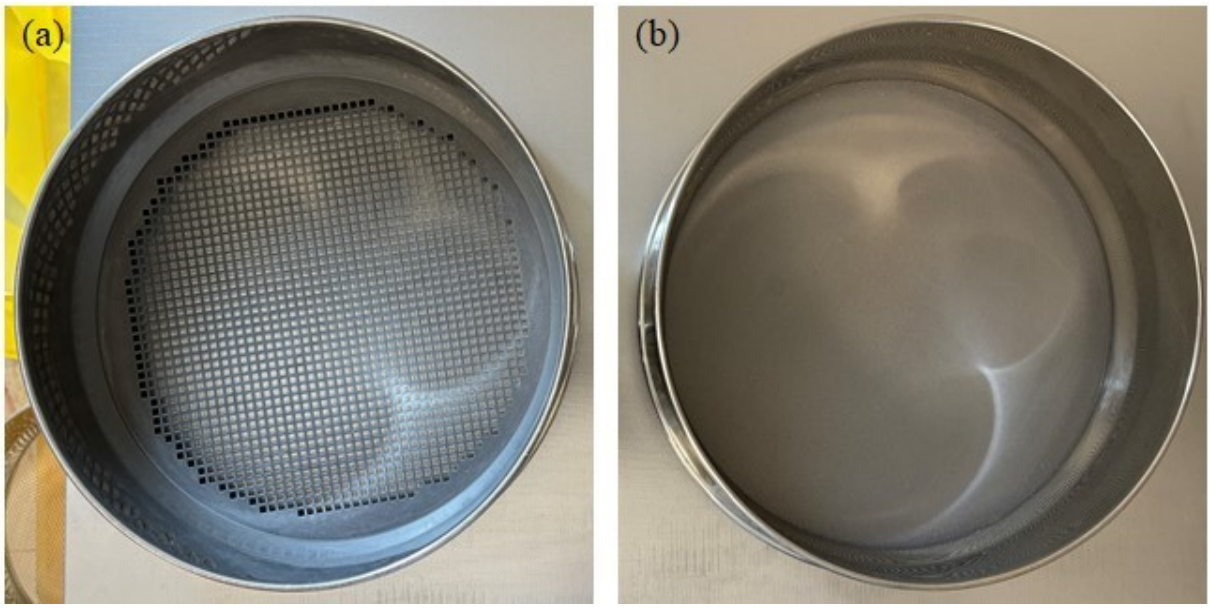

Fig. 18 Sieves utilized in the grain size sensitivity analysis; (a) 4 mm sieve, (b) 0.5 mm sieve (photos by O. Şahin).

A total of nine soil-water extracts were prepared by mixing 5 g of soil with 25 mL of deionized water, with three extracts corresponding to each grain size (0.5 mm, 2 mm, and 4 mm). This approach aimed to measure salinity three times for each soil grain size, thereby enhancing the reliability of the measurements obtained with the conductometer.

For the sensitivity analysis of soil grain size, the same procedure used in previous salinity measurements was meticulously followed. The recorded electrical conductivity values, obtained with the conductometer, are presented in Table 12 in the Results chapter.

3.5. Representation of vegetation stress using satellite data

3.5.1. Multi-spectral imagery data from Planet Scope scene

Planet Scope is a satellite technology that launched its first Dove microsatellites in 2015, followed by multiple launches in the subsequent years. These microsatellites provide daily imagery of the majority of Earth's landmass at an 3-meter spatial resolution, equipped with 4 multispectral bands including Blue (B), Green (G), Red (R), and Near-infrared (NIR), and 8 multispectral bands, which incorporate Coastal blue and Red-edge data for comprehensive analysis (Apollo Mapping, 2024).

Planet Scope is a notable satellite constellation operated by Planet, and its data serves as an excellent resource for vegetation monitoring. It complements Sentinel-2 data by providing better spatial resolution and improved temporal coverage, particularly in cloudy regions, thereby increasing the likelihood of obtaining cloud-free images (Sentinel Hub, 2024)

To download the multispectral data from the Planet Scope satellite for the study area, free of charge for the purposes of this thesis, an account was initially created on Planet's official website (Planet.com) based on information of the graduate study. A formal request for data associated with this account was subsequently submitted. During this request process, the authorities were informed that the data would be utilized for master's thesis research, and the scope, content, and focus of the thesis were explained in detail. Once the account was activated within a few days, data download activities could commence.

Table 10
Multispectral imagery data of the Planet Scope satellite from 2017 to 2024.

Date (dd/mm/yy)	Time (UTC)	Spatial Resolution (m)	Cloud Cover (%)	Area Coverage (%)	Spectral Resolution
15/08/2017	09:23:44	3	0	100	4 band
14/07/2018	0930:34	3	1	100	4 band
24/07/2019	09:54:32	3	0	100	4 band
27/07/2020	09:31:02	3	0	100	4 band
18/08/2021	09:15:34	3	0	100	4 band
08/07/2022	09:38:06	3	0	100	8 band
24/08/2023	09:48:29	3	0	100	8 band

* 4 band; Band 2: Blue, Band 3: Green, Band 4: Red, and Band 8: NIR

** 8 band; Band 1: Coastal blue, Band 2: Blue, Band 3: Green i, Band 4: Green, Band 5: Yellow, Band 6: Red, Band 7: Red-edge, and Band 8- NIR

As listed in Table 10, multi-spectral imagery for a soybean field in the commune of Porto Tolle was downloaded from the official website of the Planet data provider. This data covers a seven-year period from 2017 to 2023 and is utilized for the representation study of colour composite and NDVI.

3.5.2. Colour composites

Colour composites were generated using the QGIS tools layer. Multispectral images from 2017 to 2023, obtained from the Planet data provider, were processed individually within QGIS. Initially, the coordinates were configured to the UTM North coordinate system, EPSG: 32633-WGS 84/UTM zone 33N, for Porto Tolle, Italy. To serve as a reference for the multispectral data, Google satellite imagery was added to the Layers window in QGIS.

Since the downloaded multispectral images encompassed a significantly larger area than the study site, the first step involved narrowing the focus to the study area. This was accomplished using the 'Draw on Map Canvas' tool alongside the 'Raster', 'Extraction', and 'Clip raster by extent' features in QGIS.

Following this, a mask layer was created to delineate the study area in polygon format. This was done using the 'New Shape file Layer' feature, along with the 'Toggle editing' and 'Add Polygon feature' tools. With the mask layer established, the soybean field was clipped using the 'Raster', 'Extraction', and 'Clip raster by mask layer' functions.

The multispectral images were then displayed as RGB composites in the UTM coordinate system, utilizing various band combinations. Cartographic elements were added using 'Decorations' feature from the View menu in QGIS, including a legend, scale bar, north arrow, and grid in a zebra pattern. The final maps were scaled to 1:1875 and exported in a standard graphical format (JPG).

Different band combinations were utilized to create the colour composites based on the band order in the '3B_AnalyticMS_SR_clip' multispectral imagery data from the Planet Scope Scene. The natural colour composites, using the 3-2-1 band combination (Red-Green-Blue), provided a realistic representation of the soybean field's vegetation. In contrast, the false colour composites, using the 4-3-2 (NIR-Red-Green) and 8-7-4 (NIR-Red_{edge}-Green) band combinations enhanced the understanding of the distribution of dense and sparse vegetation. This approach facilitated a clearer assessment of vegetation presence and health. The comparison of the study area in different years against the corresponding colours in band combinations facilitated a clearer assessment of vegetation presence and health, allowing for a more accurate interpretation of the imagery.

3.5.3. NDVI computation and visualization

The Normalized Difference Vegetation Index (NDVI) is a widely used remote sensing technique that employs multispectral data to detect various land covers, including agricultural areas, vegetation indices, open spaces, and forested regions (Gandhi et al., 2015). NDVI maps are particularly valuable for assessing vegetation stress caused by soil salinity and associated land degradation. This index leverages the contrast between two spectral bands: Near-Infrared (NIR) and Red light. The red band captures the absorption of chlorophyll, while the NIR band takes advantage of the high reflectivity of plant materials. This contrast in reflectance between the Red and NIR bands allows for the observation of green vegetation's growth intensity through the spectral reflectance of solar radiation (Abdusamea, 2018).

NDVI values range from +1.0 to -1.0. Areas characterized by barren rock, sand, or snow typically exhibit very low NDVI values (0.1 or less). Sparse vegetation, such as shrubs and grasslands, or senescing crops may yield moderate NDVI values (approximately 0.2 to 0.5). In contrast, high NDVI values (approximately 0.6 to 0.9) are indicative of dense vegetation, such as that found in temperate and tropical forests or crops at their peak growth stage (USGS, 2024).

The NDVI index is computed as the follow Equation (2) and Equation (3):

$$NDVI = (NIR - R) / (NIR + R) \quad (2)$$

$$NDVI = (NIR – RE) / (NIR + RE) \quad (3)$$

Where NIR is near-infrared-band reflectance, R is red-band reflectance, and RE is red-edge-band reflectance.

For multispectral images spanning from 2017 to 2023, NDVI was computed using the 'Raster' and 'Raster Calculator' tools in QGIS. The data comprised four bands for the years 2017 to 2021 and eight bands (including the Red-edge band) for the years 2022 and 2023. Consequently, Equation (1) (Rouse Jr. et al., 1974) was applied to the four-band data, while both Equations (1) and (2) (Gitelson and Merzlyak, 1994) were utilized for the eight-band data.

In this context, NDVI computations were conducted using bands corresponding to the NIR, Red, and Red-edge bands in the multispectral imagery data from PlanetScope Scenes (refers to Table 2):

$$NDVI_{(4\text{-band})} = (Band\ 4 - Band\ 3) / (Band\ 4 + Band\ 3) \quad (4)$$

$$NDVI_{(8\text{-band})} = (Band\ 8 - Band\ 6) / (Band\ 8 + Band\ 6) \quad (5)$$

$$NDVI_{(8\text{-band})} = (Band\ 8 - Band\ 7) / (Band\ 8 + Band\ 7) \quad (6)$$

Where Band 6 is red-band reflectance, Band 7 is red-edge band reflectance, and Band 8 is near-infrared-band reflectance.

After the computations, the 'Band rendering' properties of NDVI were adjusted to enhance the realism and visualization of the results. The 'Render type' and 'Interpolation' were set to ‘Single Band pseudocolor’ and ‘Discrete’, respectively. The NDVI results, reflecting vegetation stress due to soil salinization, were represented using a ‘BrBG’ (Brown-Blue-Green) colour legend, categorized into five classes with equal intervals to effectively illustrate the natural colour variations in vegetation health.

3.5.4. NDVI computation using multi-spectral imagery data from Sentinel-2A

In this study, multispectral imagery data from the Sentinel-2A sensor were utilized to compute the Normalized Difference Vegetation Index (NDVI) for the study area. The primary objective was to compare the NDVI maps generated from multispectral data provided by both

Planet and Sentinel-2A, focusing on how the spatial resolution of these multispectral sensors impacts map production.

To initiate the analysis, the relevant multispectral imagery data were downloaded from the Copernicus database for 26 August, 2023. This dataset included images with spatial resolutions of 10 m, 30 m, and 60 m. Given that the study area encompassed a relatively small field, Bands 2 (Blue), 3 (Green), 4 (Red), and 8 (Near-Infrared) from the Sentinel-2A data, which possess a higher resolution of 10 m, were employed.

Once the bands were imported into QGIS, a virtual raster that incorporated the Red, Green, Blue, and NIR bands was created (see Fig. 19) using the 'Raster', 'Miscellaneous', and 'Build Virtual Raster' tools. To streamline the analysis, this virtual raster was clipped using the 'Draw on Map Canvas' tool, followed by the 'Raster', 'Extraction', and 'Clip Raster by Extent' functionalities, effectively reducing the size of the multispectral imagery.

Fig 19 Natural colour composite (RGB: 432) of virtual raster created using Sentinel-2A imagery data

Next, a delta mask was created to delineate the boundary of the soybean field. This was accomplished using the 'New Shapefile Layer', 'Toggle Editing', and 'Add Polygon Feature' tools in QGIS, allowing for accurate clipping of the study area from the multispectral imagery. The delta mask was then applied to extract the relevant portion of the imagery using the 'Raster', 'Extraction', and 'Clip Raster by Mask Layer' tools.

With the study area successfully clipped, the NDVI was computed with the Raster Calculator using the following formula:

NDVI = (Band 8 - Band 4) / (Band 8 + Band 4) (7)

Where Band 8 is the near-infrared reflectance and Band 4 is the red reflectance.

Upon completing the computation, the NDVI map for the soybean field was generated, which was compared with the NDVI map obtained from Planet for the same month and year (24 August 2023). This comparative analysis aims to elucidate the impact of spatial resolution on the accuracy and utility of NDVI maps in agricultural monitoring.

3.6. Drone data processing to generate the orthomosaic map

Two drone flights were conducted over the soybean field, which is the study area. The first flight took place on June 10, and the second on August 29, 2024. During these acquisition studies, multispectral images of the soybean field were captured. The collected imagery was processed using Agisoft Metashape Pro software to produce an orthomosaic map, which was then used to evaluate vegetation stress related to soil salinity through NDVI computations.

On June 10, the soybean plants were not yet mature; since the presence of vegetation is a crucial factor in NDVI index computations, a second acquisition was performed on August 29 when the plants had reached maturity. While the flight details for the June 10, 2024, drone operation are provided in Table 11 and Table 12, the flight details for August 29 could not be presented because the data from that date is still being processed.

Table 11
Drone flight details for the first imagery acquisition conducted on June 10, 2024.

Imagery data	Number of images	Flying altitude (m)	Ground resolution (cm/px)	Coverage area (km^2)	Tie points	Projection	Reprojection error (px)
Multispectral	1,504	53	2.41	0.0824	380,579	4,381,284	0.732
D (RGB)	376	57.8	1.42	0.0936	178,924	1,330,346	0.814

Table 12
Resolution details of the imagery data of the first acquisition on 10 June 2024.

Camera Model	Resolution
M3M, D (RGB)	5280 x 3956
M3M, Green	2592 x 1944
M3M, Red	2592 x 1944
M3M, Red_{edge}	2592 x 1944
M3M, NIR	2592 x 1944

The process of creating the orthomosaic map from the drone-captured multispectral imagery in Agisoft Metashape Pro began with meticulous data preparation. First, high-quality multispectral images were collected from a drone equipped with appropriate sensors. These images covered various wavelengths, including D (RGB) and the multispectral bands such as Green (G), Red (R), Red_{edge} (RE), and Near-infrared (NIR). After acquiring the imagery, the

files were systematically organized separately into the project folders for the RGB and the multispectral photos, facilitating easy access during the processing stages.

RGB image data were used to create one orthomosaic map representing the natural colour composition of the soybean field, while multispectral image data were utilized to generate another orthomosaic map for NDVI computation.

Once the data was organized, the images were imported into Metashape by navigating to the "Workflow" menu and selecting "Add Photos" dialog browse. During import, the images were designated as captured with a "Single cameras" a necessary specification based on the imaging setup to ensure proper processing of the RGB image data. Conversely, the multispectral images were imported using the "Multi-camera system" data layout, allowing Metashape to automatically arrange the bands according to the information in the image metadata.

Subsequently, the next critical step involved aligning the photos, which was achieved by selecting "Align Photos" from the "Workflow" menu. During this alignment process, the software analysed the imagery and generated a sparse point cloud representation of the scene. Point clouds are essential in this study as they provide a detailed representation of the spatial relationships and surface structures within the soybean field, which is crucial for understanding vegetation health and soil conditions.

After aligning the images, a 2D model was created by selecting "Build Model" from the "Workflow" menu, using "Tie Points" as the source data. Tie points are critical for establishing correspondences between overlapping images, enabling the software to accurately align and georeference them. While a 2D model provides a flattened representation of the landscape, it can still enhance the analytical capabilities of remote sensing data by allowing for detailed measurements and assessments. Once the model was established, a texture was applied to the 2D model by selecting "Build Texture" from the "Workflow" menu to enhance the visual quality, detail, and analytical value of the orthomosaic map.

The final step involved creating the orthomosaic. This was accomplished by selecting "Create Orthomosaic" in the "Workflow" menu. The orthomosaic type was set to "Reflectance," enabling the software to compute NDVI and effectively analyse vegetation stress. The projection was then adjusted to align with the geographical coordinate system of the study area.

Once the orthomosaic was completed, the NDVI index was computed in Metashape software using the orthomosaic map generated from the multispectral band data. This was done by selecting the "Raster Calculator" from the "Tools" menu. In the Raster Calculator dialog box, the NDVI formula as shown in Equation 8 was applied through the "Set Raster Transform" option. The computation used the Red (R) and Near Infrared (NIR) bands from the source data, as specified in the Transform tab.

$$NDVI = (Band\ 4 - Band\ 2) / (Band\ 4 + Band\ 2) \quad (8)$$

Where Band 2 is red-band reflectance and Band 4 is near-infrared band reflectance.

Finally, to ensure that the orthomosaic maps retain the same number of bands as the source data before export, the Raster Transform section was set to "None" and the "Export Orthomosaic" option was selected, enabling the results of the orthomosaic creation to be exported in TIFF format.

CHAPTER 4: RESULTS

4.1. Laboratory analysis

The values obtained from salinity measurements of the soil/water extracts, prepared over a two-day laboratory study, were recorded according to the depth of the soil samples collected from various sampling points.

In addition to the salinity measurements, sensitivity analysis was conducted to evaluate how grain size affects salinity levels in the extract for the sample exhibiting the highest salinity. The results of this analysis were categorized according to grain size.

The recorded salinity values are detailed in Section 4.1.1, while the results of the sensitivity analysis are presented in Section 4.1.2. Furthermore, the findings are enhanced with graphs based on the average salinity values from the sampling points.

4.1.1. Salinity level of soil samples

As shown in Table 13, the salinity measurements of soil/water extracts prepared from samples collected at sampling points 2, 3, 4, and 50 (see Fig. 20) indicate that the actual soil salinity (EC_e) values in the soybean field, selected as the study area, range from 1.63 to 9.98 dS/m. Additionally, these values vary with increasing soil depth at the sampling points.

Table 13

Salinity levels for $EC_{1:5}$ (µS/cm and dS/m) and EC_e in (dS/m) recorded at each sample point, categorised by depth.

Sample point	Depth (cm)	$EC_{1:5}$ (µS/cm)	$EC_{1:5}$ (dS/m)	EC_e (dS/m)	Average EC_e (dS/m)
2	Soil surface	325.00	0.33	2.84	3.27
	44.2-56	326.00	0.33	2.84	
	80-85	415.00	0.42	3.61	
	145-155	441.00	0.44	3.78	
3	Soil surface	415.00	0.42	3.61	5.82
	45-55	590.00	0.59	5.07	
	90-100	1,018.00	1.02	8.77	
4	Soil surface	626.00	0.63	5.42	7.05
	45-55	665.00	0.67	5.76	
	70-80	1,158.00	1.16	9.98	
50	Soil surface	191.00	0.19	1.63	2.15
	45-50	196.00	0.20	1.72	
	63-73	355.00	0.36	3.10	

* The depth of soil samples collected from the soil surface varies between 0-10 cm.

** Multiplication factor is 8.6 for light clays

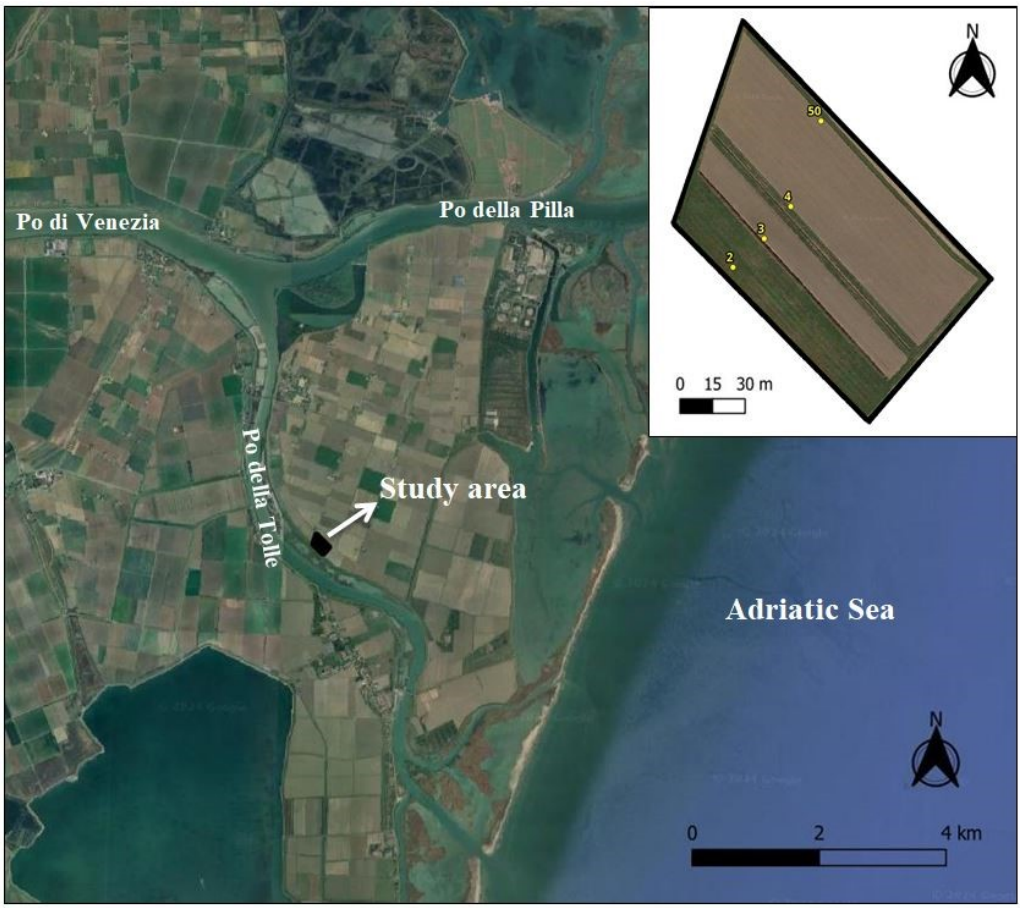

Fig 20 The study area is situated near the Po della Tolle branch within the Po River Delta, utilizing QGIS and projected in the WGS84 and UTM coordinate systems on Google Satellite imagery. In the upper right corner, a map of the soybean field is displayed, highlighting the locations of the sampling points.

The lowest EC_e values were recorded at sampling point 50, while point 2 exhibited slightly higher salinity levels, though still close to those of point 50. The measurements from sampling points 3 and 4 reveal that, although the salinity levels at these points are close, sampling point 4 has the highest salinity levels, ranging from 5.42 to 9.98 dS/m.

Fig. 21 illustrates the variation of EC_e values with soil depth for each sampling point, clearly showing an increase in salinity levels as soil depth increases.

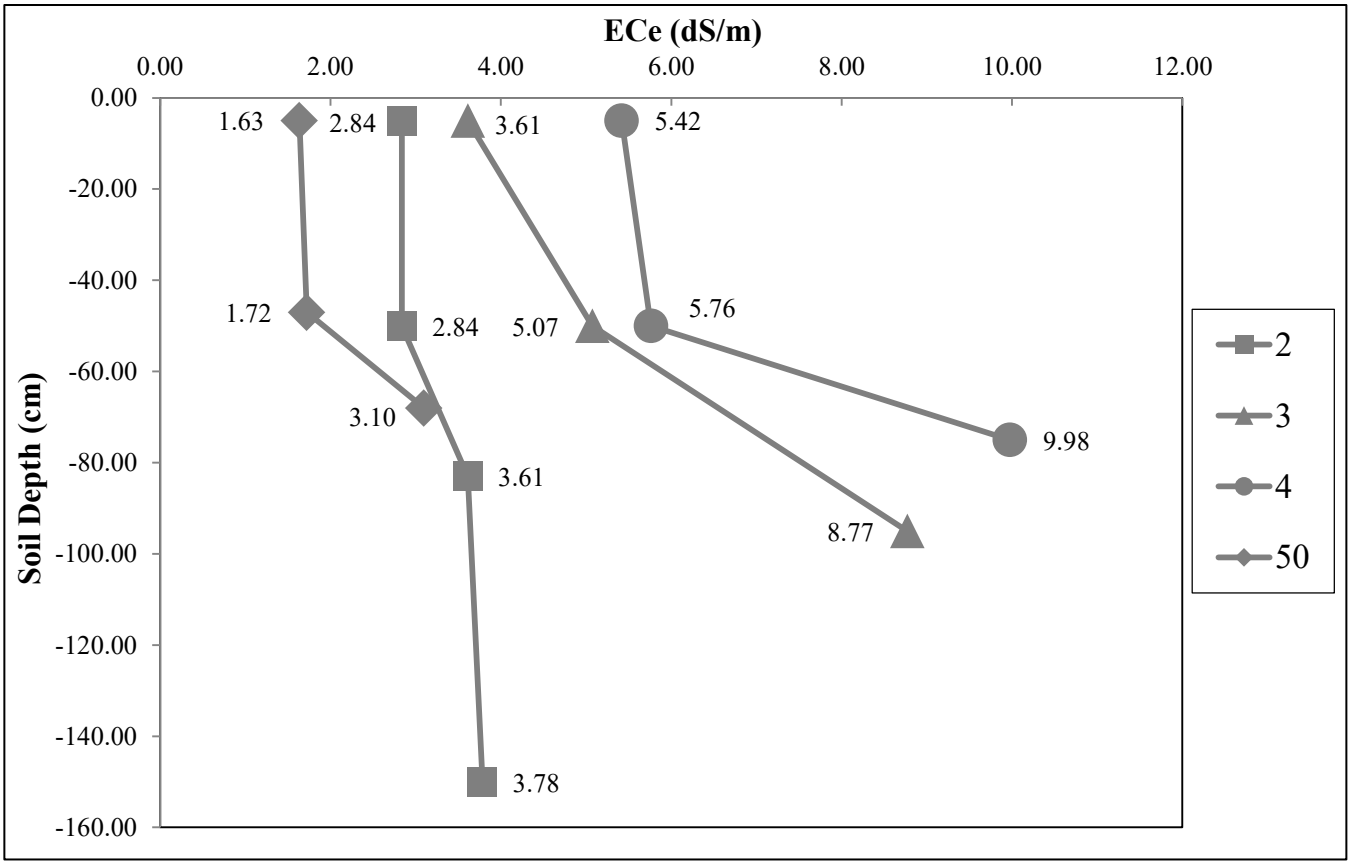

Fig. 21 Actual soil salinity (EC_e) values of the samples on sampling points based on soil depths

The actual soil salinity (EC_e) recorded from samples collected at various depths from the same sampling point were averaged (see Table 11). This process was applied to calculate the average soil salinity for each sampling point. The variations in average soil salinity in relation to surface elevation and distance from the river are illustrated in Figures 22 and 23, respectively.

Although the soybean field is relatively flat, the surface elevations of sampling points 2, 3, 4, and 50 are 1.93, 2.1, 2.2, and 2.2 meters below sea level, respectively. Figure 22 illustrates that sampling points 2 and 3, which are situated at higher elevations, contrast with points 50 and 4, which are at lower elevations. Despite being at similar heights, sampling point 50 exhibits the lowest average soil salinity, while point 4 has the highest.

Figure 23 indicates that the average soil salinity value for sampling point 2, located closest to the river at a distance of 79 meters, is intermediate compared to the other points. In contrast, the average salinity for point 50, which is the furthest from the river at 228 meters, is the lowest.

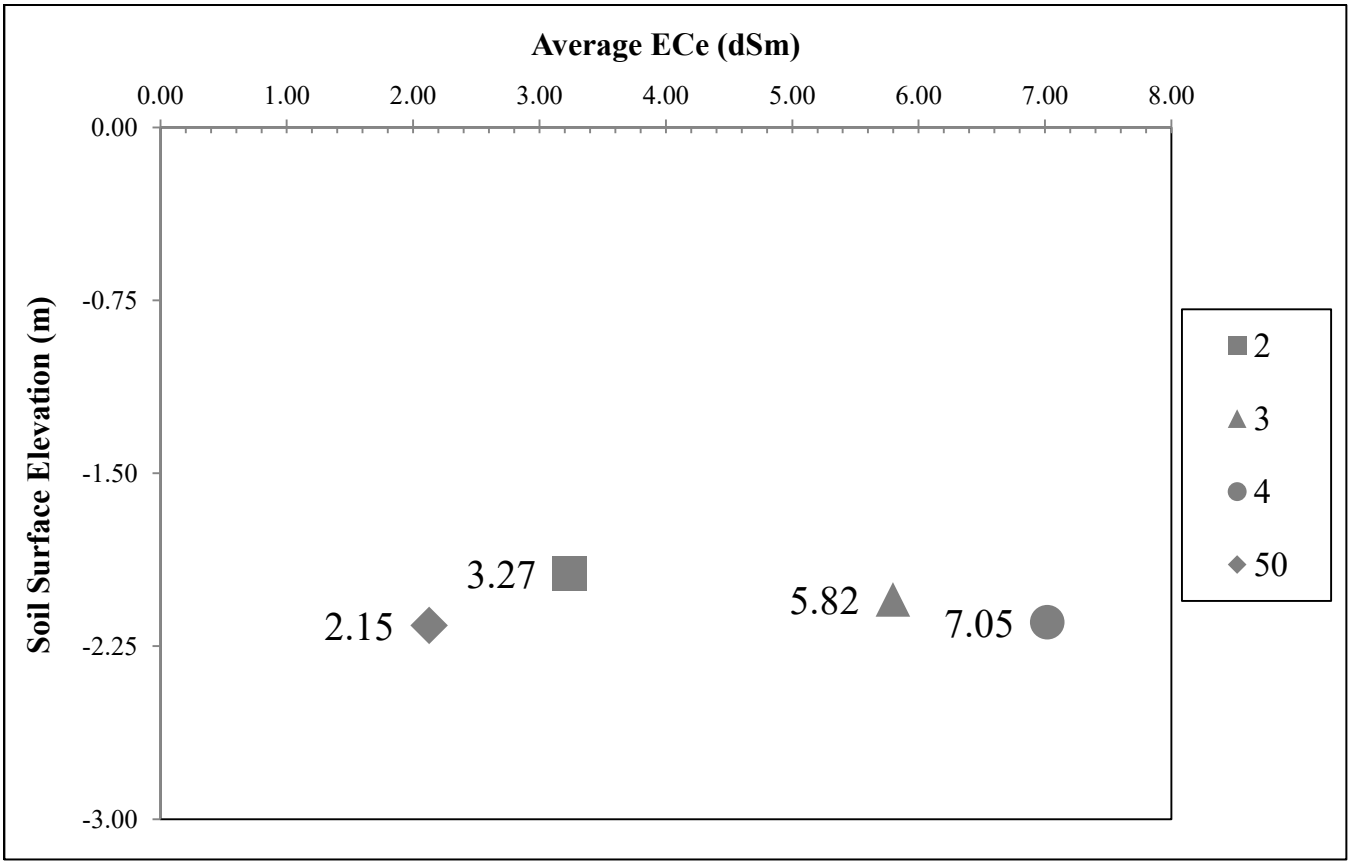

Fig. 22 Average actual soil salinity (EC_e) values of the samples on sampling points based on soil surface elevation

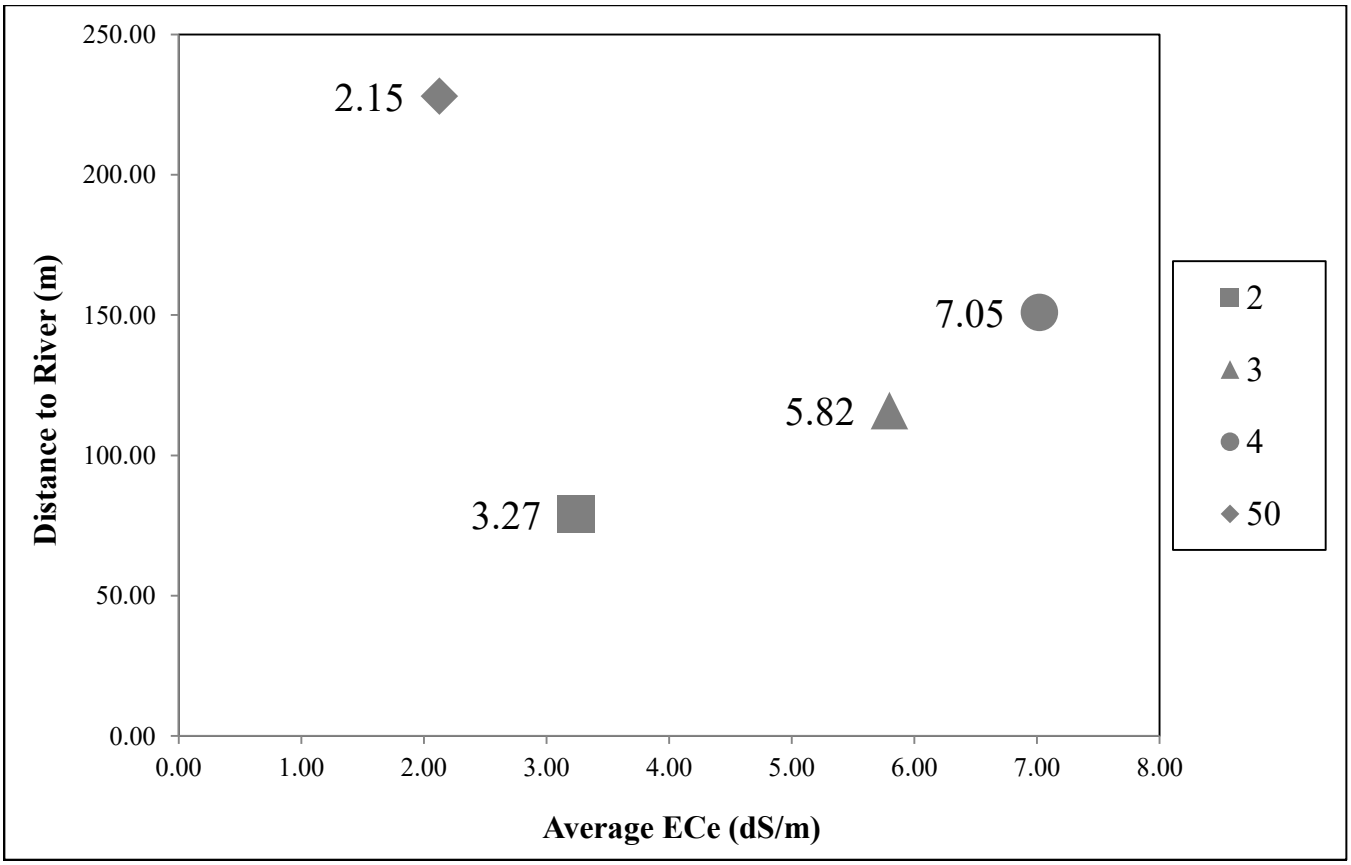

Fig. 23 Average actual soil salinity (EC_e) values of the samples on sampling points based on distance to river

4.1.2. Sensitivity analysis for grain size

Based on the measurements conducted, the soil sample taken from a depth of 70-80 cm at sampling point 4 exhibited the highest salinity value, recorded at 9.6 dS/m. To assess the impact of grain size on salinity levels in soil/water extracts, samples were passed through 0.5 mm, 2 mm, and 4 mm sieves. The resulting soil salinity values from these measurements are presented in Table 14.

Table 14

Salinity levels for $EC_{1:5}$ (µS/cm and dS/m) and EC_e in (dS/m) recorded through grain size sensitivity analysis for the soil sample collected from a depth of 70-80 cm at sample point 4, which exhibited the highest salinity measurements

Sieve size (mm)	Measurement No.	$EC_{1:5}$ (µS/cm)	$EC_{1:5}$ (dS/m)	EC_e (dS/m)	Average EC_e (dS/m)
0.5	1	1,105.00	1.105	9.503	7.63
	2	795.00	0.795	6.837	
	3	762.00	0.762	6.553	
2.00	1	1,158.00	1.158	9.958	7.93
	2	780.00	0.780	6.708	
	3	830.00	0.830	7.138	
4.00	1	1,049.00	1.049	9.021	7.30
	2	845.00	0.845	7.267	
	3	654.00	0.654	5.624	

As shown in Table 14, the extract prepared from the 2 mm grain size soil sample had the highest average salinity value of 7.93 dS/m, while the extract derived from the 4 mm grain size soil sample had the lowest average salinity value of 7.30 dS/m. Sensitivity analysis indicates that the extracts prepared with the three different grain sizes yielded average soil salinity values that are very close to one another.

4.2. Salinity mapping using remote sensing technologies

Multispectral imagery of soya bean, which is the study area, were downloaded from Planet Scope data provider for the years 2017-2023 and these downloaded data were processed in QGIS and MetaShape software and mapping studies based on colour composite and NDVI index computation were carried out to determine the vegetation stress caused by soil salinity.

The results obtained from the colour composite studies are presented in section 4.2.1, and the results of the salinity mapping studies based on NDVI index are presented under 4.2.2 and 4.2.3 under separate headings as satellite and drone based, respectively, according to the remote sensing technology used.

4.2.1. Colour composites

The natural colour band combination of a soybean field is shown by 3-2-1 (Red-Green-Blue). This combination is based on visible bands. Therefore, objects and land cover types resemble their visible appearance: dense vegetation is dark green and is represented by light shades of green according to plant health. Dry vegetation is brown, while bare soil is represented by varying shades of white. Although the natural band combination is mostly used for urban areas, it can give an idea of the vegetation density of agricultural land.

Band combination of 4-3-2 (NIR-Red-Green) includes the infra-red bands which is advantageous for vegetation. This band combination is the most effective for agricultural mapping and vegetation studies due to the effective distinguishability of colour showing land cover types and vegetation health in contrasting colours. In this band combination, healthy vegetation has a darker red hue, while lighter colours indicate sparsely vegetated areas because plants reflect near infrared and green light, while absorbing red. Since they reflect more near infrared than green, plant-covered land appears deep red. Denser plant growth is darker red. Bare soils, which lack vegetation, are represented by cyan (a greenish-blue colour) because they reflect more incidents light in certain wavelengths, particularly in the absence of vegetation.

In addition, the 8-7-4 (NIR-Red_{edge}-Green) band combination for the 2022 and 2023 data, which consists of eight bands, was prepared to assess vegetation density and health. The Red-edge band was favoured in this analysis due to its sensitivity to subtle changes in chlorophyll content and plant stress. This band can detect nuanced variations in vegetation reflectance that indicate stress or the early stages of senescence.

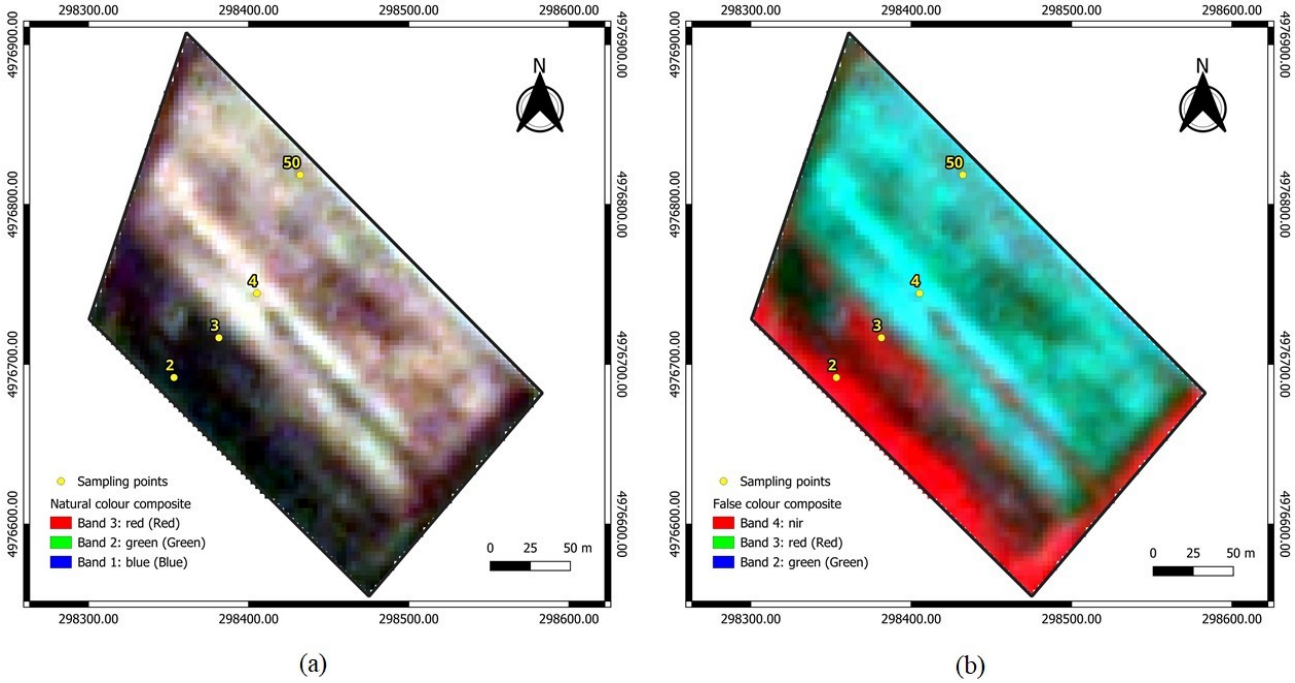

Fig. 24 Colour composites of the field using Planet Scope multispectral data from August 2017; (a) 3-2-1 (Red-Green-Blue) and (b) 4-3-2 (NIR-Red-Green)

As seen in Fig. 24(a) in the natural colour composite, the area surrounding sampling point 2 displays dark green tones, indicating healthy and dense vegetation with adequate moisture and nutrients. Similarly, sampling point 3 is located near the center of field, where white tones predominate but are surrounded by dark green hues. At sampling point 4, the green tones are significantly diminished, remaining within the white-toned area, which suggests a lack of healthy vegetation and possible bare soil or stressed plants. Meanwhile, sampling point 50 is situated in an area with green tones, although not as pronounced as those at points 2 and 3.

In the false colour composite Fig. 24(b), the area surrounding sampling point 2 is bright red, indicating dense, healthy vegetation and confirming the observations made in the natural colour composite. Sampling point 3 also appears in a red hue, indicating dense vegetation and further supporting the conclusion of healthy plant life in this region. In contrast, sampling point 4 is represented in a cyan colour, indicating bare soil or a lack of healthy vegetation. Sampling point 50 is located within an area represented by a transition between green and cyan colours.

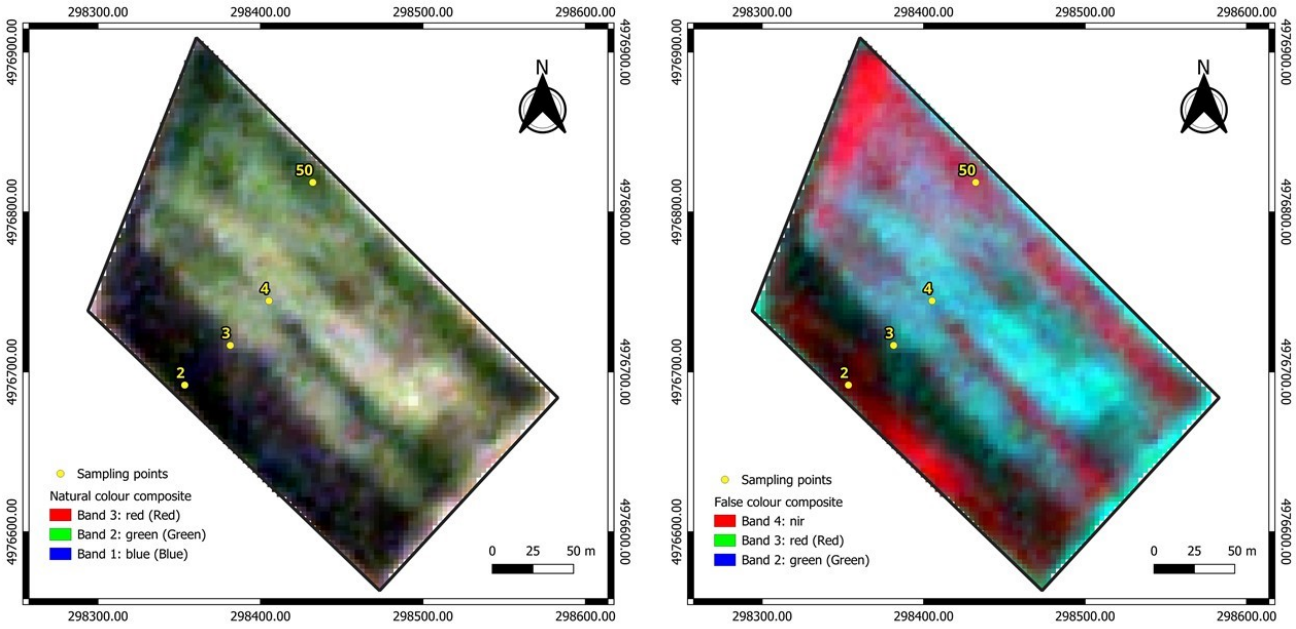

Fig. 25 Colour composites of the field using Planet Scope multispectral data from July 2018; (a) 3-2-1 (Red-Green-Blue) and (b) 4-3-2 (NIR-Red-Green)

In Fig. 25(a), sampling point 2 is situated within a dark green area, signifying healthy and dense vegetation. Sampling point 3 is found in a region of healthy vegetation characterized by a transition from dark green to lighter green tones. The area surrounding sampling point 4 exhibits less green and more brown or yellow hues, indicating a mix of colours that suggests stressed or sparse vegetation. Point 50 is similar to Point 2, but displays a lighter green, suggesting moderate vegetation health.

In in Fig. 25(b), the area in which point 2 is located demonstrates greater intensity in the red colour tones, indicating enhanced vegetation health or density compared to the other points. Point 4 appears muted in the cyan colour tones, which aligns with observations from the

natural colour composite and indicates that the vegetation is stressed or sparse. Point 3 is located at the border of dense and healthy vegetation. Sampling point 50 exhibits moderate reflectance in the red colour tones, suggesting the presence of medium-density vegetation like point 2.

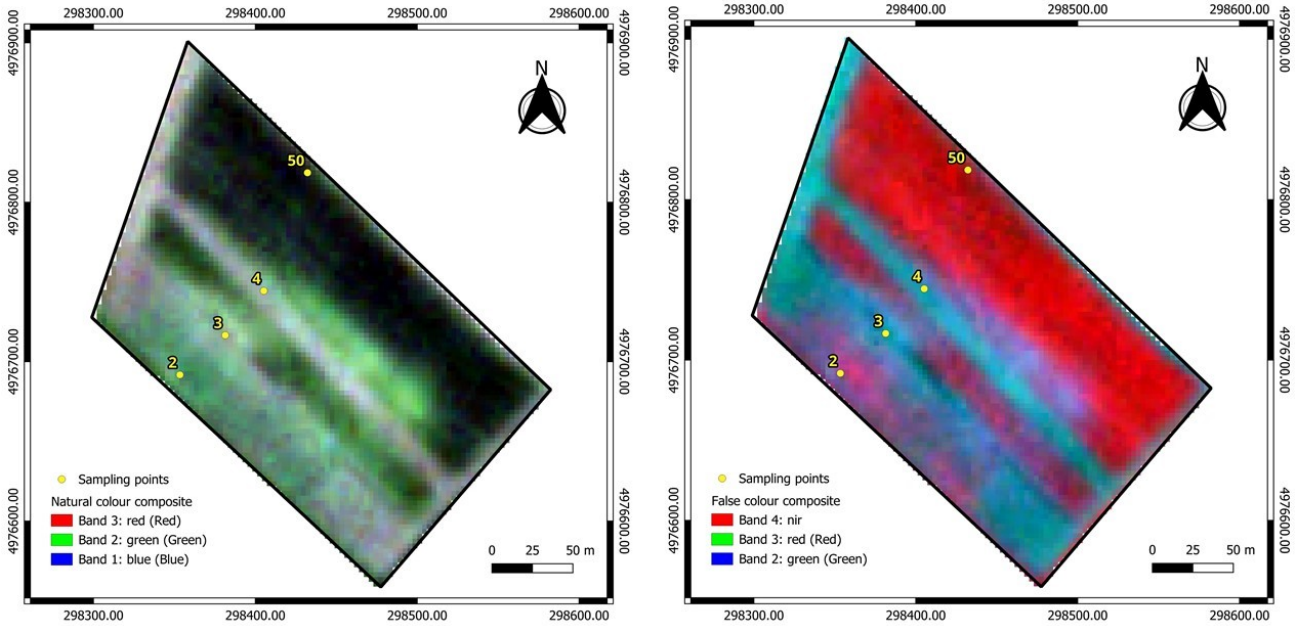

Fig. 26 Colour composites of the field using Planet Scope multispectral data from July 2019; (a) 3-2-1 (Red-Green-Blue) and (b) 4-3-2 (NIR-Red-Green)

Fig. 26(a) illustrates that, although sampling point 2 is situated in a darker green area compared to points 3 and 4, the latter sampling points are found in regions where shades of green are less prevalent. This suggests the presence of sparse and moderately healthy vegetation surrounding these locations. In contrast, sampling point 50 is positioned in an area characterized by darker green, indicating dense and healthy vegetation.

In Fig. 26(b), sampling point 50 is located in the dark red area, while point 2 is situated in a lighter red zone, and points 3 and 4 are found in regions dominated by shades of cyan. This representation confirms the natural colour composition.

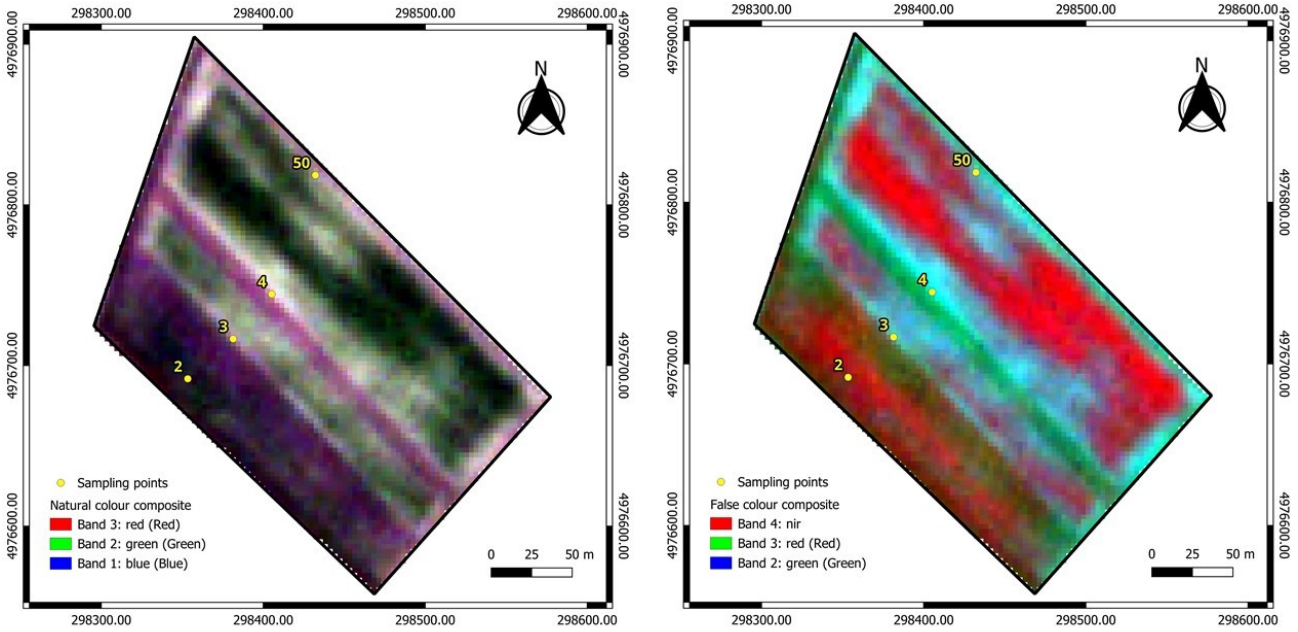

Fig. 27 Colour composites of the field using Planet Scope multispectral data from July 2020; (a) 3-2-1 (Red-Green-Blue) and (b) 4-3-2 (NIR-Red-Green)

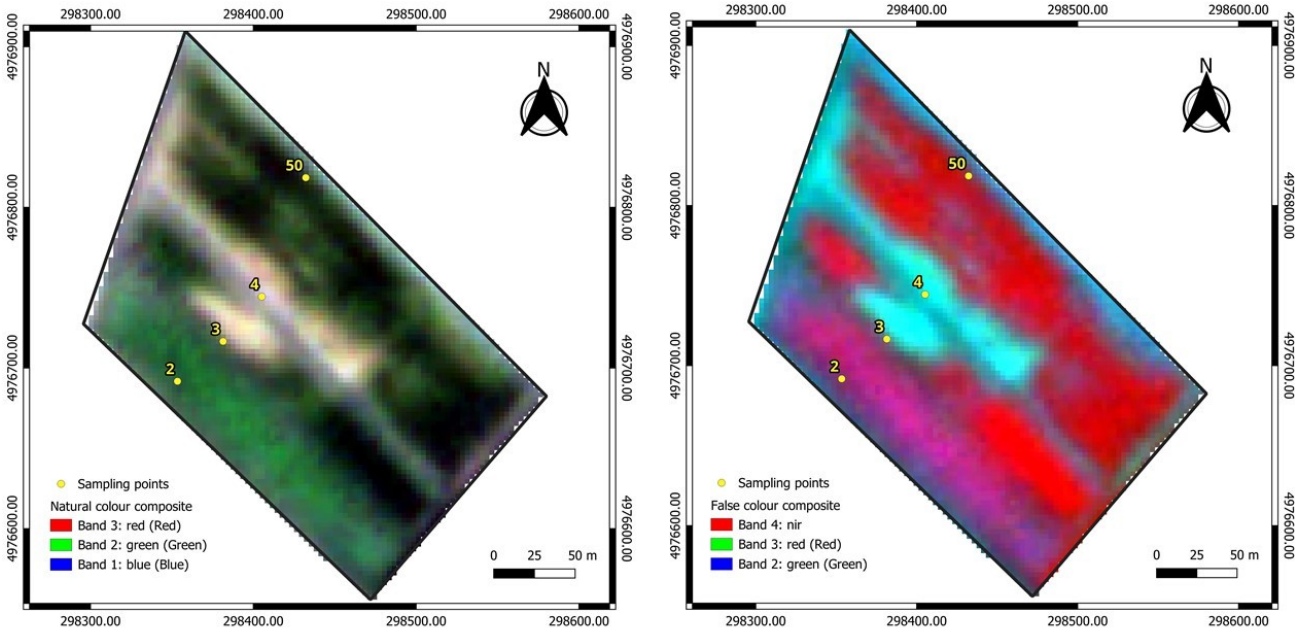

Fig. 28 Colour composites of the field using Planet Scope multispectral data from August 2021; (a) 3-2-1 (Red-Green-Blue) and (b) 4-3-2 (NIR-Red-Green)

Natural colour composites, as illustrated in Fig. 27(a) and in Fig. 28(a), indicate that sampling points 2 and 50 are situated in regions characterized by dark green colour tones. Conversely, the sampling points 3 and 4 are found in areas devoid of vegetation, which are predominantly represented by white and orange hues.

In Fig. 27(b) and Fig. 28(b), which depict false colour composites, it is evident that sampling points 2 and 50 are encircled by areas dominated by red tones, signifying dense and healthy vegetation. In contrast, sampling points 3 and 4 are surrounded by cyan tones.

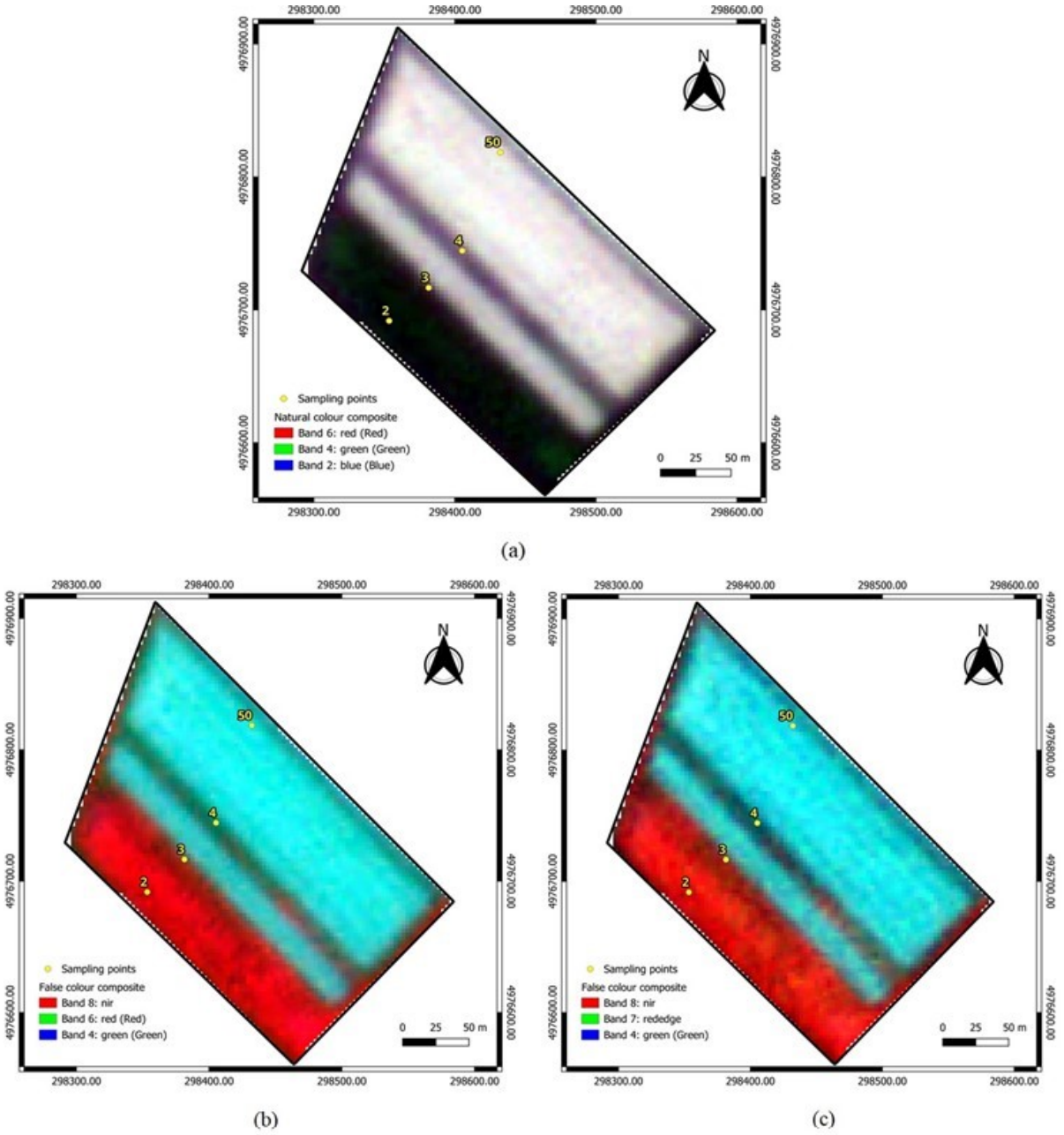

Fig. 29 Colour composites of the field using Planet Scope multispectral data from July 2022; (a) 3-2-1 (Red-Green-Blue), (b) 4-3-2 (NIR-Red-Green), and c) 8-7-4 (NIR-Red_{edge}-Green)

As depicted in Fig. 29(a), there was no cultivation activity in the field in July 2022, as the soybean soil was predominantly bare. However, Fig. 29(b) reveals that the areas surrounding sampling point 2 is represented by a dark red colour.

In Fig. 29(c), the Red-edge band was utilized instead of the standard Red band to assess the impact of Red-edge band reflection on the depiction of plant health and density. This figure

demonstrates the red colour tone transitions in the areas encompassing sampling point 2 at a higher resolution due to the use of the Red-edge band.

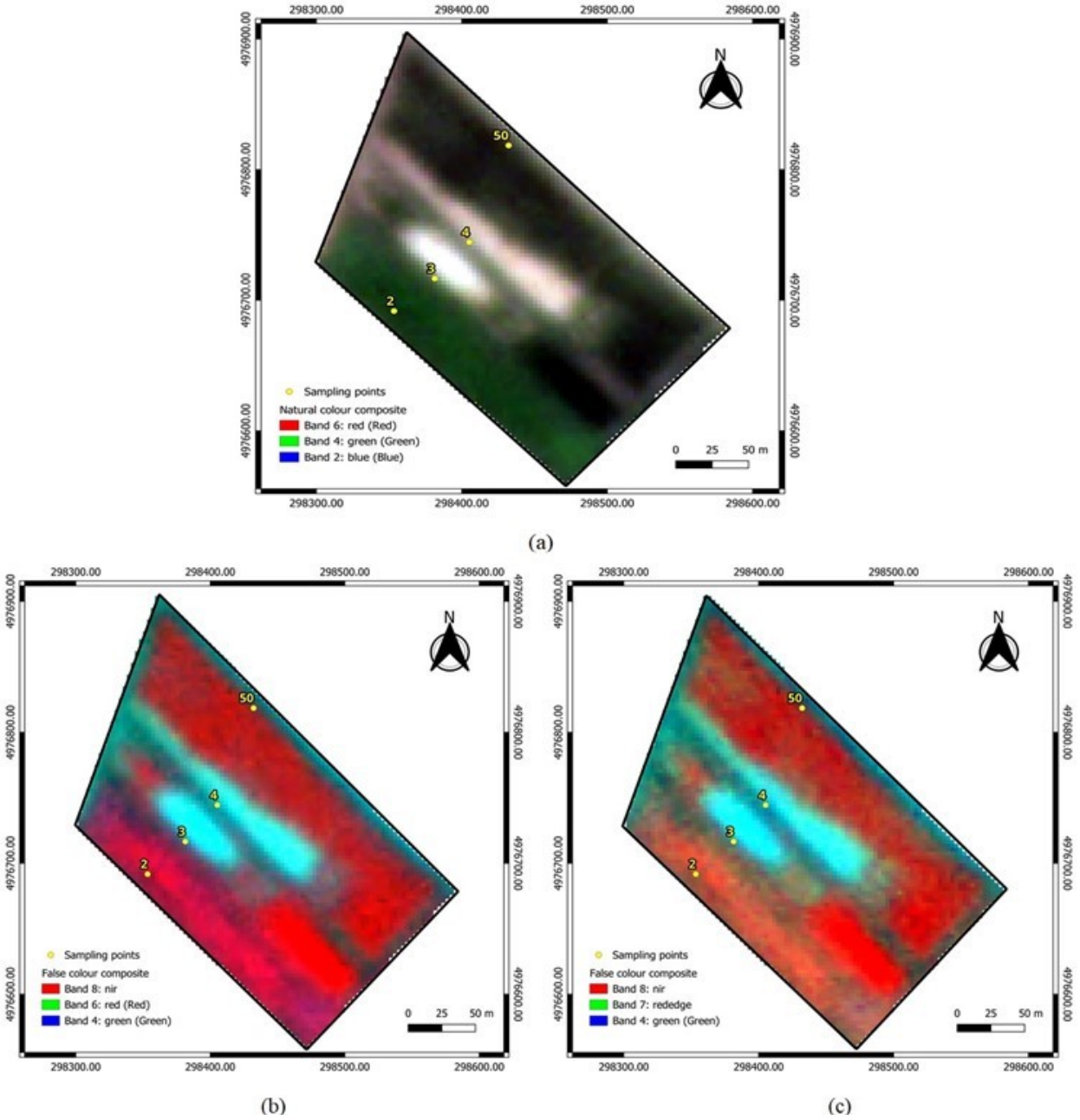

Fig. 30 Colour composites of the field using Planet Scope multispectral data from August 2023; (a) 3-2-1 (Red-Green-Blue), (b) 4-3-2 (NIR-Red-Green), and c) 8-7-4 (NIR-Red_{edge}-Green)

Fig. 30 presents colour composites, including natural, red, and Red-edge bands, derived from an image of a soybean field taken in the final days of August 2023. In Fig. 29(a), dense and healthy vegetation is indicated by dark green in the areas surrounding sampling points 2 and 50, while the vicinity of sampling point 4 is shown in white and orange tones, signifying bare soil.

The false colour composites of 2023 are presented in Fig. 30(a) and Fig. 30(b). In Fig. 30(b), dense and healthy vegetation is represented by red colour tones and bare soil is represented by

cyan colour tones. In Fig. 30(c), by using the Red-edge band shows that the vegetation health and density are represented by more detailed colour transitions

4.2.2. NDVI maps using satellite-based remote sensing technology

NDVI maps present a clear visualization of vegetation density and health based on vegetation stress due to soil salinity were generated by calculating the NDVI index for each year of soya bean data. The NDVI (Normalized Difference Vegetation Index) index is presented in 5 different value ranges: less or equal than 0.5, 0.5-0.6, 0.6-0.7, 0.7-0.8 and greater than 0.8 and each range is represented by colours appropriate to the nature of plant health.

Brown (NDVI <= 0.5): This colour represents areas with low vegetation density or unhealthy vegetation.

Light Brown (NDVI = 0.5 - 0.6): This range indicates moderate vegetation density, suggesting healthier vegetation than the brown areas but still not optimal.

Beige (NDVI = 0.6 - 0.7): Representing fairly healthy vegetation, this colour denotes a good level of vegetation density.

Light Green (NDVI = 0.7 - 0.8): This colour signifies healthy and dense vegetation, indicating a thriving ecosystem.

Dark Green (NDVI > 0.8): This represents areas of very high vegetation density, typically indicating lush, healthy plant growth.

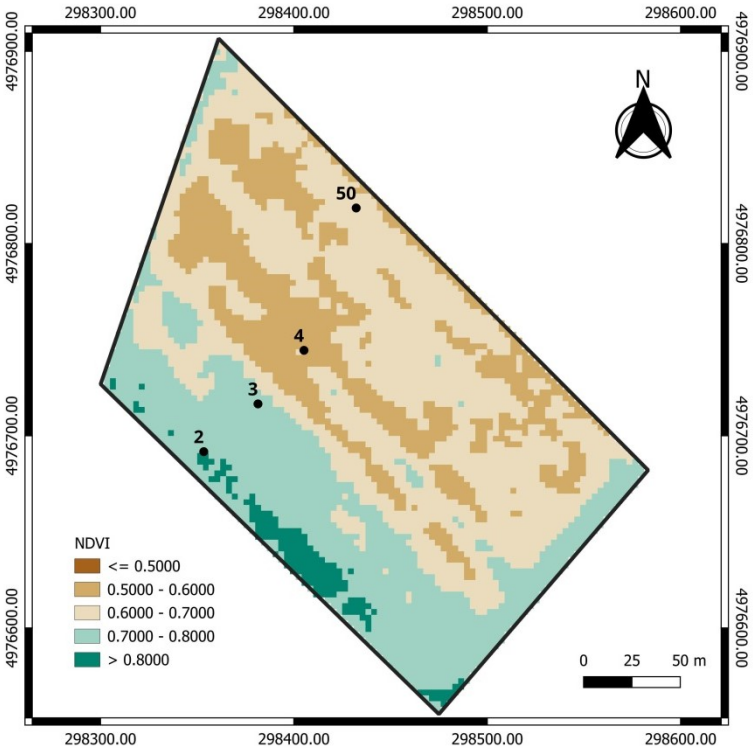

Fig. 31 NDVI (computation includes NIR and Red bands) map of the field using Planet Scope multispectral data from August 2017

In Fig. 31 of the soybean field for 2017, sampling points 2 and 3 are situated within the light green region. The calculated NDVI value, ranging from 0.7 to 0.8, suggests the presence of healthy and dense vegetation in this area. Sampling point 50 is found in the beige region, which corresponds to a value range of 0.6 to 0.7, while sampling point 4 is located in the light brown area, which extends significantly, particularly in the central sections of the soybean field. This indicates that the vegetation in this region exhibits average health and density.

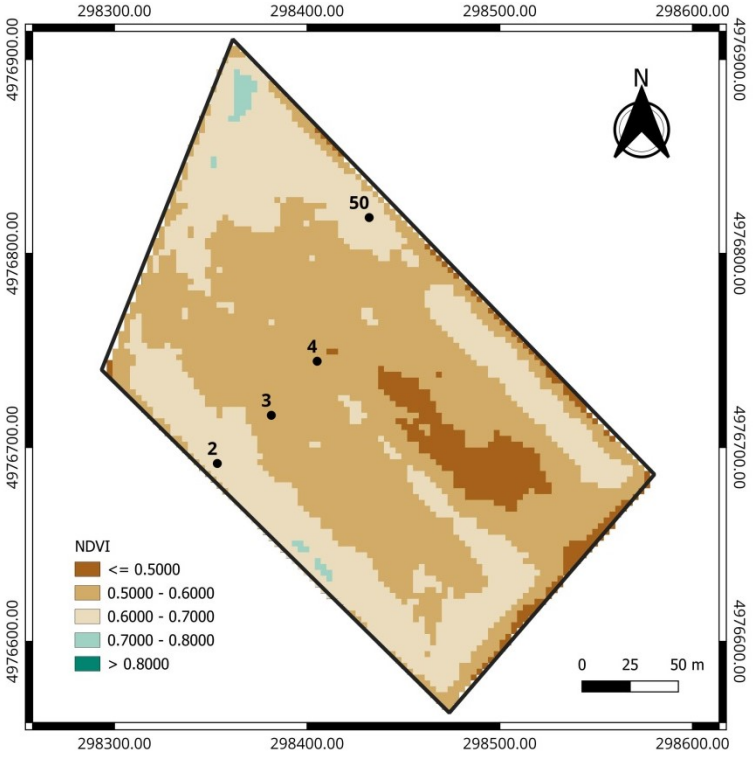

Fig. 32 NDVI (computation includes NIR and Red bands) map of the field using Planet Scope multispectral data from July 2018

Fig. 32 illustrates the results obtained from the 2018 data. For this year, the soybean field predominantly appeared light brown. This colour representation suggests that the vegetation health and density were moderate, with sampling points 3 and 4 located within this area.

Sampling points 2 and 50 position in the beige region, which signifies healthy vegetation along the edges of the field. Additionally, Fig. 24 reveals a small area of low-health vegetation, depicted in dark brown, situated near sampling point 4.

In Fig. 33, which presents the results from the 2019 data, the light green colour representation, encompassing sampling point 3 and covering nearly half of the soybean field, is particularly noteworthy. This area, where the NDVI value ranges from 0.7 to 0.8, indicates the presence of healthy and dense vegetation.

Sampling points 3 and 4 are located in areas represented by light brown, signifying low vegetation health and density in those regions. Sampling point 2 is also found at the boundary between the light green and beige areas, indicating that the vegetation surrounding this point is healthy and dense.

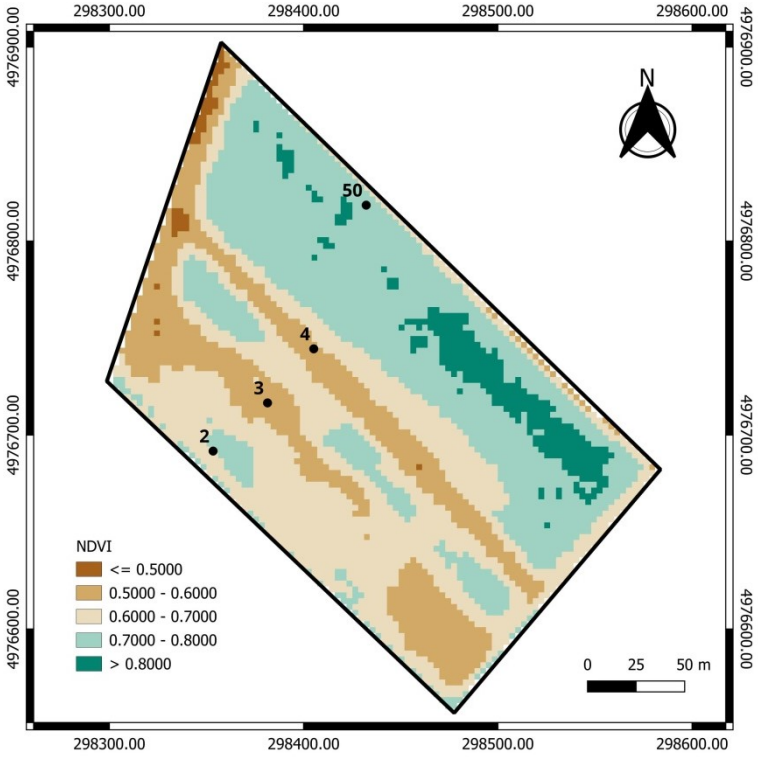

Fig. 33 NDVI (computation includes NIR and Red bands) map of the field using Planet Scope multispectral data from July 2019

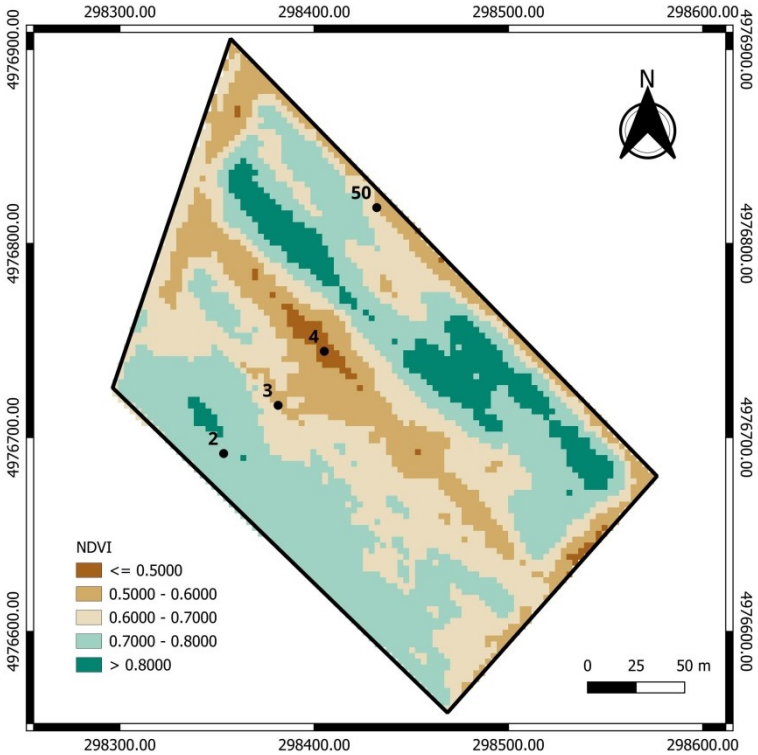

Fig. 34 NDVI (computation includes NIR and Red bands) map of the field using Planet Scope multispectral data from July 2020

Fig. 34 displays the results obtained from the soybean field data in 2020. The colour representation indicates slightly dark brown in the central areas surrounding sampling point 4, and light brown around sampling point 3, covering a broad area. The calculated NDVI value of less than 0.6 suggests that plant health is low and plant density is sparse in these regions.

The light and dark brown areas are encircled by beige, indicating that low-health vegetation is bordered by healthy and dense vegetation.

Furthermore, the presence of light and dark green areas, particularly along the horizontal edges of the field, signifies dense vegetation with good to high health levels. Sampling point 2 is situated within this thriving area, while point 50 is located outside of it, in a region characterized by moderate vegetation density and health.

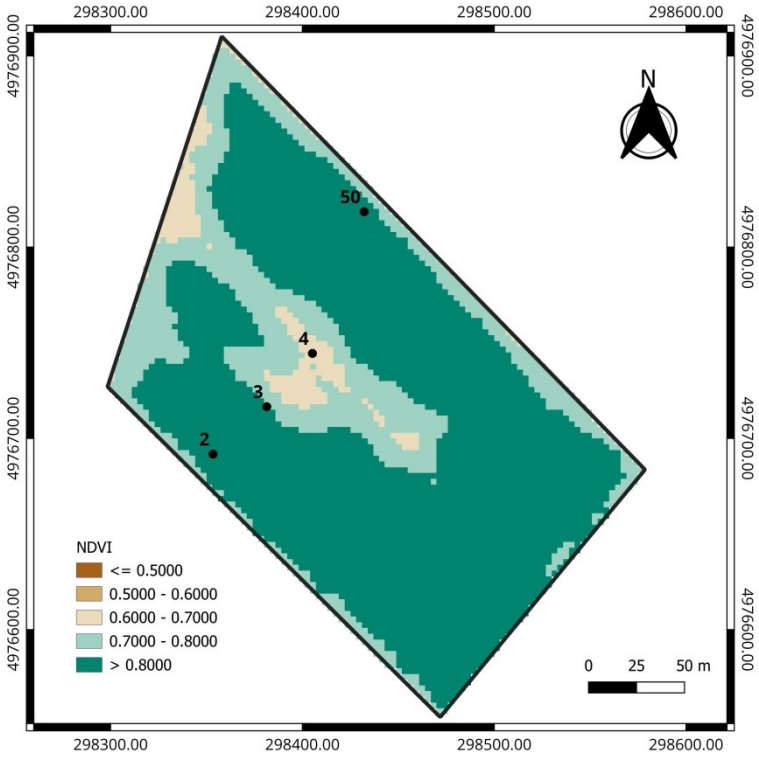

Fig. 35 NDVI (computation includes NIR and Red bands) map of the field using Planet Scope multispectral data from August 2021

Fig. 35 illustrates the results obtained from the soybean field data for 2021.

As shown in Fig. 35, the field is predominantly covered in dark green, which represents NDVI values greater than 0.8. This indicates a high presence of healthy and dense vegetation in the soybean field. Sampling points 2, 3, and 50 are located within this area of robust vegetation.

However, there is a beige-coloured area in the central part of the field that includes sampling point 4, despite the large presence of healthy and dense vegetation in the field. This beige area has an NDVI value ranging from 0.6 to 0.7, indicating vegetation of moderate health and density.

Fig. 36 and Fig. 37 illustrate the results obtained from the data collected in 2022 and 2023, respectively. These multispectral imagery datasets allow the calculation of NDVI using Red_{edge} band instead of the traditional Red band because of they consist 8 bands, which include also the Red_{edge} band. The maps generated using the Red-edge bands are displayed in Fig. 35(b) and Fig. 36(b).

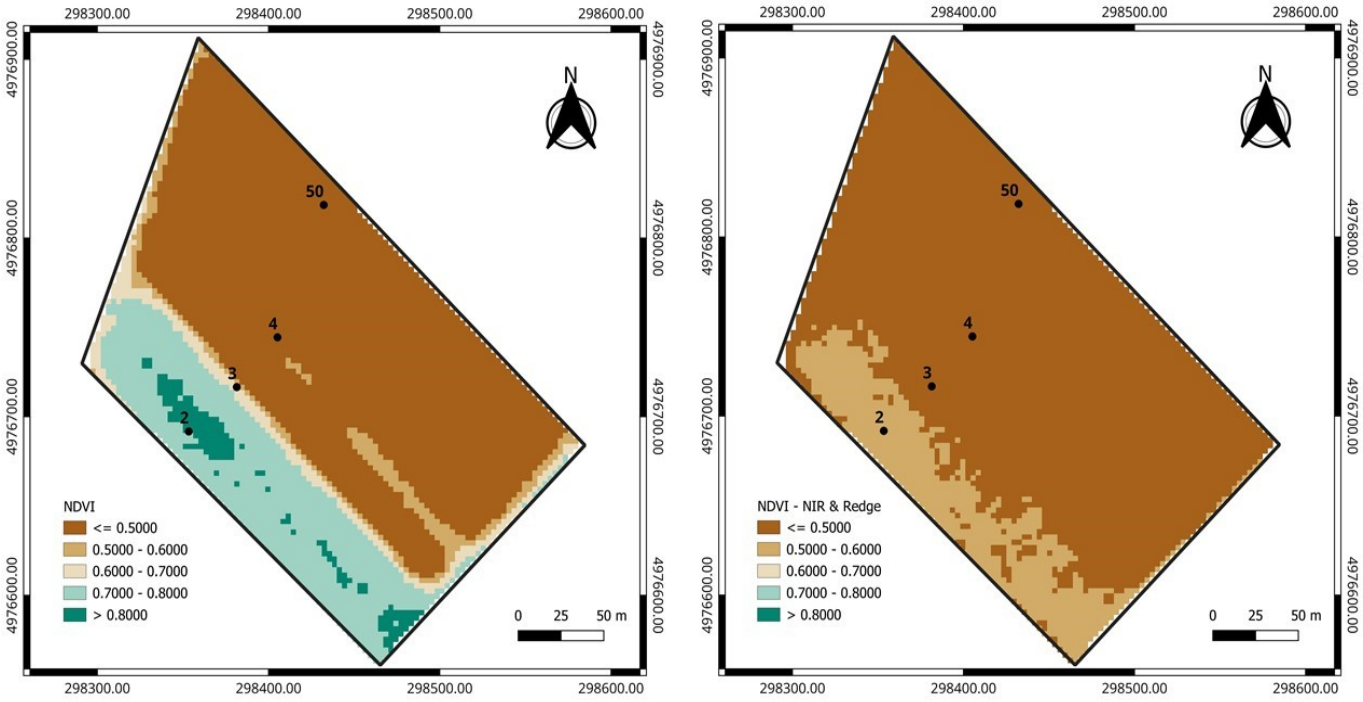

Fig. 36 NDVI maps of the field using Planet Scope band data from July 2022; (a) using NIR and Red bands and (b) using NIR and Red_{edge} bands

In Fig. 36(a), it is evident that the majority of the soybean field is depicted in a dark brown colour, indicating that the field was not cultivated in 2022. While this colour suggests the presence of unhealthy and sparse vegetation, it is clear that these areas represent bare soil due to the lack of cultivation. Conversely, similar to previous years, presence of healthy and dense vegetation are visible, represented by light green and dark green hues, particularly at area surrounded sampling point 2 within the agricultural area and extending throughout the field.

Fig. 36(b) reveals that the areas shown in light and dark green in Fig. 35(a) are depicted in light brown. For these regions, the NDVI values calculated using the Red_{edge} band range between 0.5 and 0.6. These findings indicate that the NDVI values derived from the Red_{edge} band are lower than those calculated using the Red band.

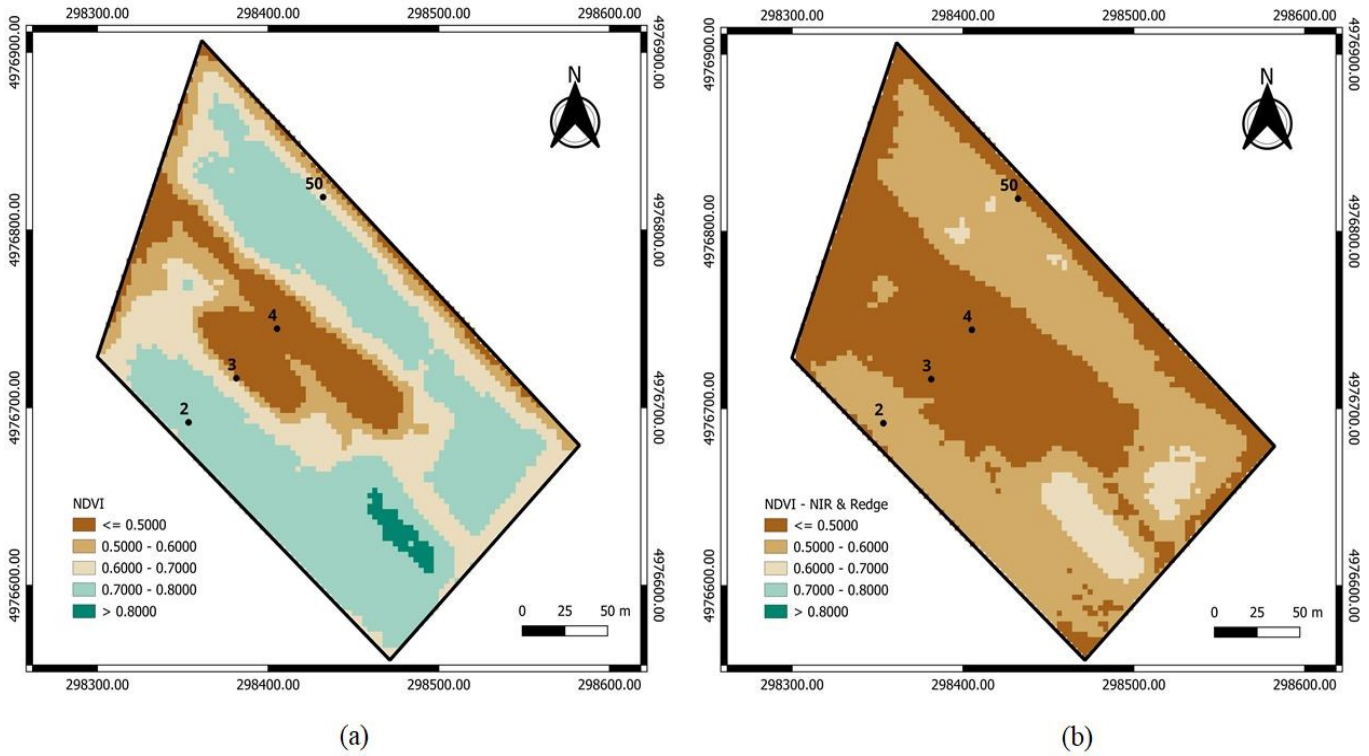

Fig. 37 NDVI maps of the field using Planet Scope multispectral data from August 2022; (a) using NIR and Red bands and (b) using NIR and Red_{edge} bands

In Fig. 37(a), the presence of unhealthy and sparse vegetation is seen, represented by dark brown, covering the central portion of the soybean field. Surrounding this area, a substantial portion of the field is covered by healthy and dense vegetation, indicated by light green.

Fig. 37(b) presents similar results to those shown in Fig. 36(b), confirming that the NDVI values calculated with the Red-edge band are lower. Additionally, in both Figures 37(a) and (b), it is noted that the sampling points fall within regions characterized by unhealthy and sparse vegetation, consistent with the findings from previous years.

4.2.2.1. Comparison of NDVI maps resolution between Planet Scope and Sentinel sensors

The NDVI map generated using multispectral imagery of the study area from the Sentinel-2A sensor in August 2023 was compared to the map produced from Planet Scope data on the same date (see Fig. 38).

The two maps presented in Fig. 38 depict NDVI (Normalized Difference Vegetation Index) values for a soybean field, with the Sentinel-2A multispectral data shown on the left and the Planet Scope Scene multispectral data on the right. The Sentinel-2A map, which has a spatial resolution of 10 meters, displayed less detailed NDVI patterns, indicative of the coarser resolution associated with this dataset. This lower resolution resulted in a broader, less defined range of NDVI values, failing to capture finer variations within the field.

In contrast, the Planet Scope Scene map displayed a smoother and more continuous distribution of NDVI values, attributed to its higher spatial resolution of 3 meters. This

increased resolution facilitated more precise detection of variations within the field, resulting in a more detailed NDVI map with a narrower and more specific range of values.

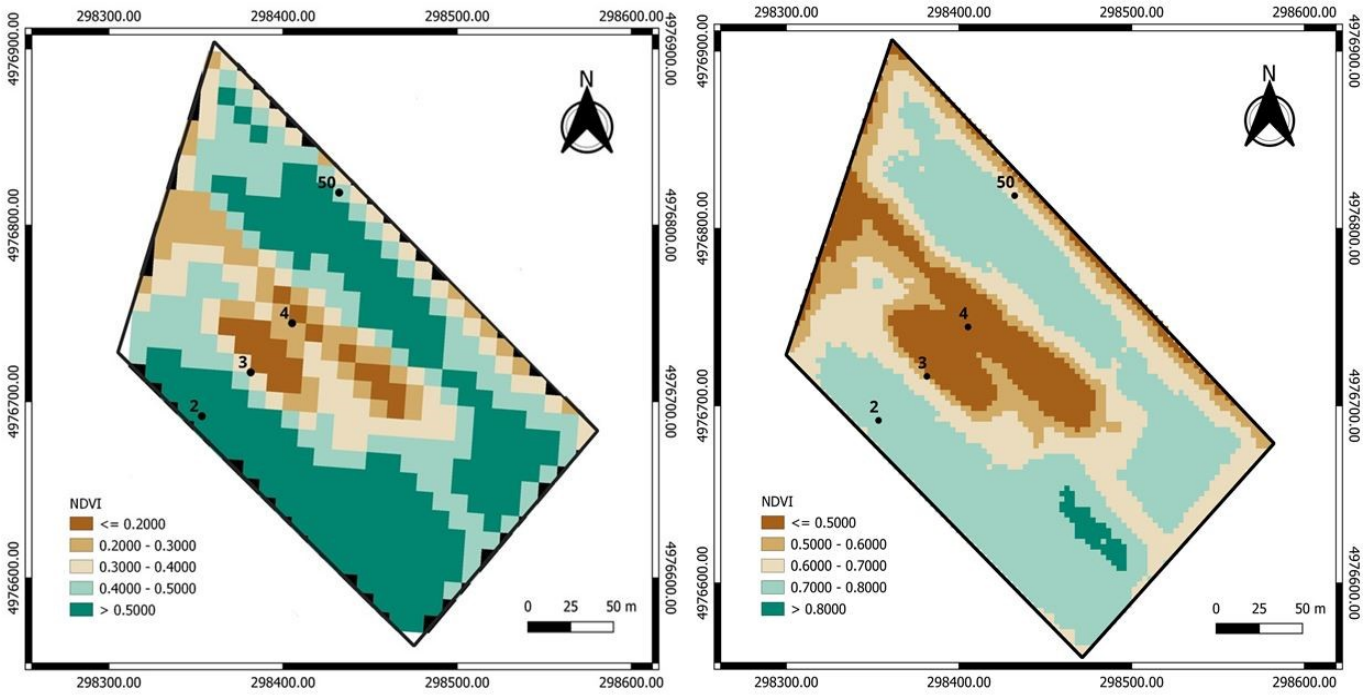

Fig. 38 Comparison of NDVI maps of the the field using multispectral data from August 2023 of different sensors; (a) Sentinel-2A and (b) Planet Scope scene

The Sentinel-2A map shows less than or equal to 0.2 to greater than 0.5, with most of the field exhibiting values between 0.3000 and 0.5000, suggesting moderate vegetation health. Some areas display lower NDVI values, potentially indicating regions of stress and reduced vegetation density. However, this broader range and the less distinct variation in values are a consequence of the lower spatial resolution of the Sentinel-2A data. Conversely, the Planet Scope Scene map features a higher NDVI range, from less than or equal to 0.5 to greater than 0.8, reflecting a more detailed and accurate assessment of vegetation health across the field. The enhanced resolution of the Planet Scope Scene data allowed for improved detection of variations, resulting in a clearer and more refined NDVI map.

4.2.2.2. Comparison of NDVI index values at sampling points corresponding to the years from 2017 to 2023

NDVI (Normalized Difference Vegetation Index) is a key indicator of vegetation health, where higher values reflect healthier, denser vegetation, and lower values indicate sparser vegetation, often associated with dry or drought conditions. In this section, NDVI indices computed in QGIS for the seven years (2017-2023) using multispectral data obtained from Planet Scene Scope were compared. The NDVI values for each sampling point during this period are depicted in the graph shown in Fig. 39, providing a comparative view of vegetation health trends over the years.

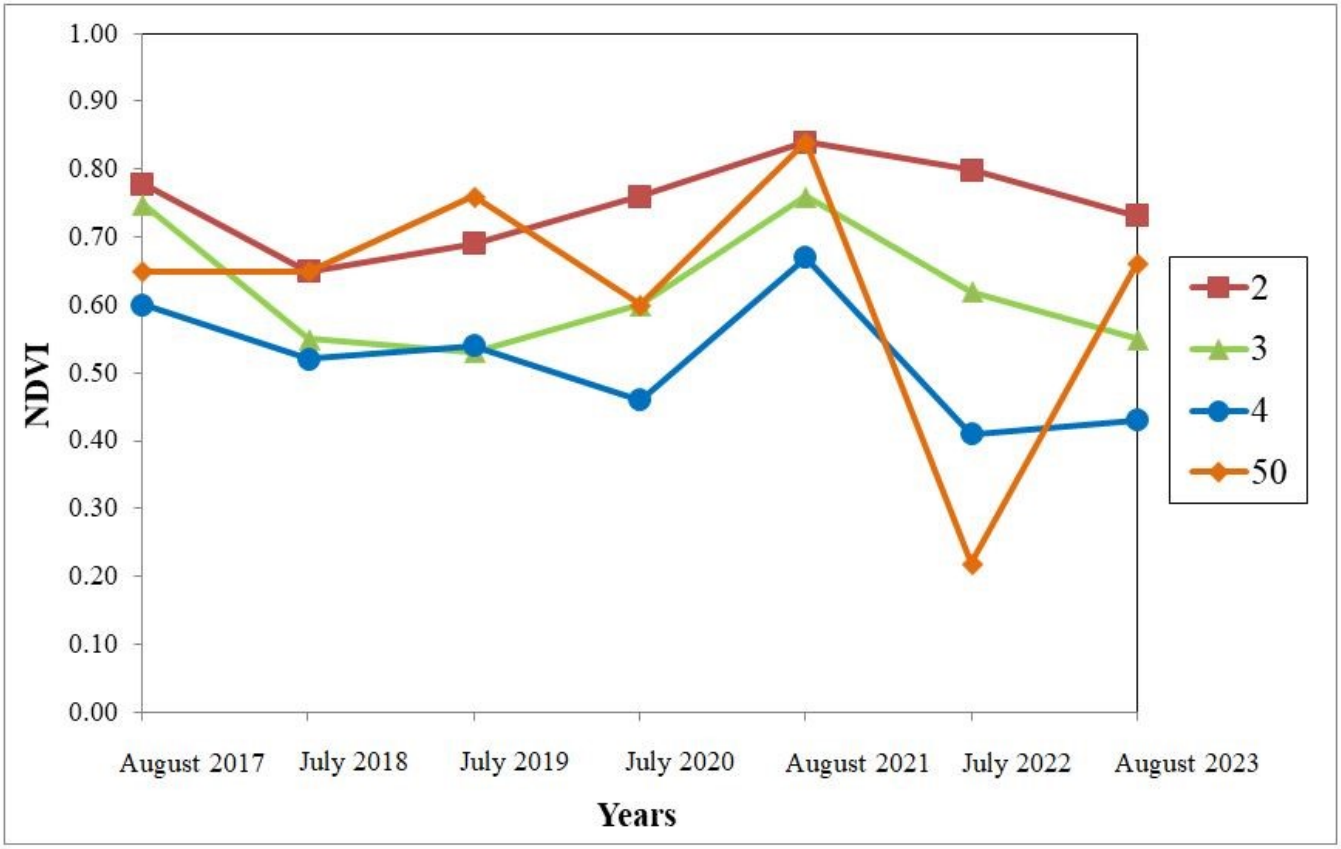

Fig. 39 Comparison of NDVI indices for sampling points from 2017 to 2023, based on multispectral data from Planet Scope.

Fig. 39 displays the Normalized Difference Vegetation Index (NDVI) values from 2017 to 2023 for four different sampling points, 2, 3, 4, and 50.

The NDVI values are influenced by both the crop type and the time of year. For instance, in July, soybean plants are typically small, whereas by August they approach maturity. Given that the field has been annually rotated among Soybean, Corn, and Wheat since 2017, this rotation likely contributes to the observed interannual variability in NDVI values, reflecting changes in biomass associated with different crops.

The significant rise in NDVI values from 2020 to 2021 across all sampling points suggests a period of healthier vegetation, likely due to favourable growing conditions. However, the expected signal of the drought conditions during 2021-2022 is not evident in the NDVI data, which may be attributed to the irrigation practices or the influence of river water seepage. Although irrigation was not reported, the reliance on river water, even when saline during seawater intrusion, could have mitigated the impact of drought conditions on crop growth.

The observed drought conditions around 2017, 2019, and particularly 2022 are consistent with the NDVI trends, with wetter conditions noted around 2020-2021. The decline in NDVI values towards 2023 indicates a return to less favourable conditions for vegetation growth. The variability in NDVI is also influenced by annual crop rotation and fluctuations in rainfall and river levels, which affect biomass and, consequently, NDVI values.

4.2.3. NDVI maps using drone-based remote sensing technology

Two distinct types of orthomosaic maps were generated from the acquisition of D (RGB) and multispectral (G, R, RE, and NIR) image data, obtained through drone flights (see Table 11) over the soybean field. The orthomosaic map created using D (RGB) band data provided a natural color composite representation of the soybean field, while the map produced with multispectral band data was utilized to calculate the NDVI, allowing for the assessment of vegetation health and density in relation to soil salinity. As previously mentioned, since the data acquired on August 29 are still being processed, only the map results generated from the June 10 data are presented in this section.

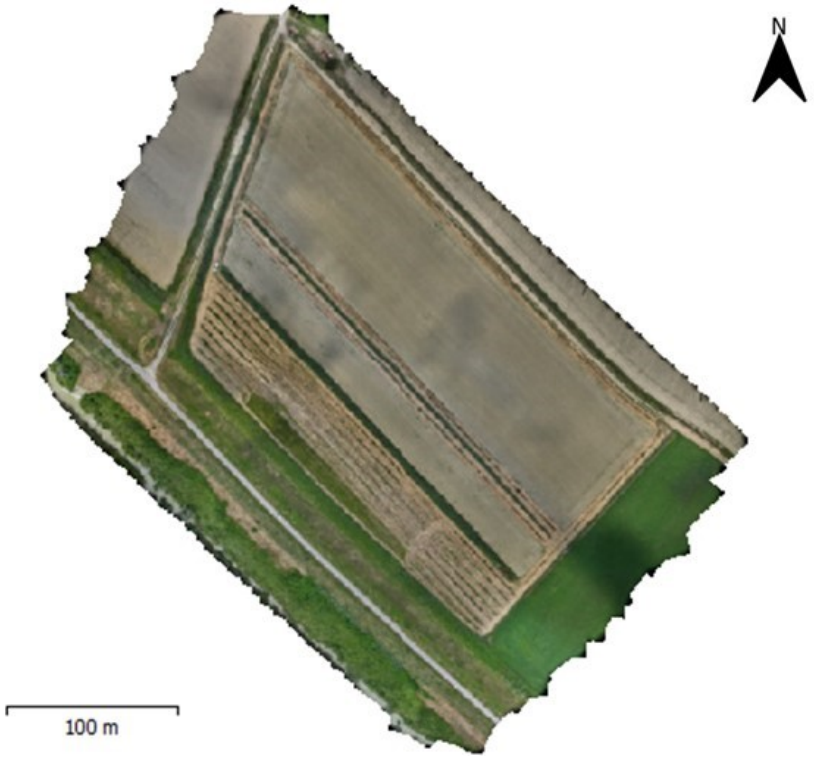

Fig. 40 Natural colour composite of soybean field generated using RGB bands in Agisoft Metashape Pro.

Fig. 40 depicts a natural colour composite of the soybean field. The field appears mostly bare, as soybean plants are still very small in early of June. In contrast, the presence of fully developed vegetation in the areas surrounding the study site is clearly visible in the natural colour composite of the produced orthomosaic map.

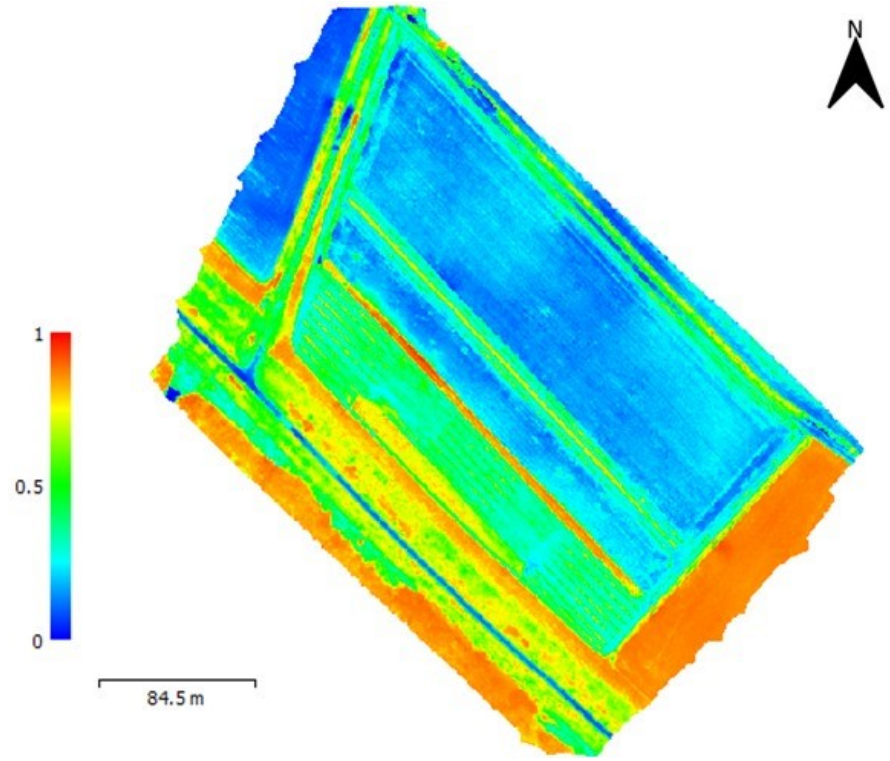

Fig. 41 NDVI map of soybean field generated using multispectral band (Red and Near-infrared) data in Agisoft Metashape Pro.

Fig. 41 displays the NDVI map of the soybean field, which is used to assess the density and health of the vegetation affected by soil salinization. Since the vegetation in the field is not yet mature, the NDVI index for the study area is represented by blue tones, indicating values of 0 and those close to zero. The vegetation in the areas surrounding the soybean field is represented by yellow and orange colours, corresponding to NDVI index values of 0.7 to 0.8, respectively.

CHAPTER 5: DISCUSSION

The objective of this thesis is to investigate the characterization of salinity-affected agricultural areas in the Po River Delta using a combination of in situ observations and remote sensing techniques. The research seeks to determine the impact of soil salinity on vegetation stress in these areas and to explore effective methods for mapping salinity-affected regions through satellite and drone-based remote sensing technologies, supported by laboratory data.

This thesis study focuses on a soybean field located in the Po Delta region near Porto Tolle, where soil salinity has been documented previously. The land affected by soil salinity was mapped through fieldwork, laboratory analyses, and satellite and drone-based remote sensing technologies.

A total of 13 soil samples were collected from four different points within the agricultural land, as part of the soil salinity assessment of the selected soybean field. The study was conducted by preparing Soil/Water extracts, a widely used method for determining soil salinity, as described in the 'Literature Review' chapter of the thesis. The electrical conductivity of these extracts was measured. Electrical conductivity measurements were taken from Soil/Water extracts prepared at a ratio of 1 to 5, following the methodology outlined by Hardie and Doyle (2012). The values were recorded in µS/m and converted to dS/m using the conversion coefficient provided by Gibbs (2000), as referenced in current literature, and presented in Table 12 of the 'Results' chapter.

It is well established that soil salinity levels generally increase with depth in areas affected by saline water intrusion. The laboratory analyses confirmed that salinity levels increased with depth, aligning with findings in the Po River Delta, where saltwater intrusion during drought conditions led to significant soil salinization, particularly in areas closer to the sea (Luo et al., 2020). This process is driven by the upward movement of saltwater from the underground, which contributes to higher salinity levels deeper in the soil profile. The highest electrical conductivity values recorded were 8.77 dS/m and 9.98 dS/m, obtained from extracts of samples collected at depths of 95 cm at sampling point 3 and 85 cm at sampling point 4, respectively. According to Brown et al. (1954), soils with electrical conductivity values ranging from 8 to 16 dS/m are classified as 'strongly saline soils.' This indicates that sampling points 3 and 4, located in the center of the selected soybean field, contain soil affected by salinity at this level.

The measurements performed yielded electrical conductivity (EC_e) values of extracts prepared from samples mostly below 4 dS/m. According to the laboratory results, these EC levels indicate that the agricultural land selected as the study area is moderately affected by salinization. This level of salinity poses a significant threat to soybean cultivation, as soybean is a sensitive crop with with low salinity tolerance. Typically, EC_e values between 2 and 4 dS/m suggest that only moderately salt-tolerant crops can be grown without substantial yield reduction, highlighting the potential risk to soybean production in this area.

The literature review conducted revealed that satellite-based remote sensing is widely used in studies of salinity-affected lands, with mapping efforts utilizing multispectral image data

collected from these sensors. In light of this information, multispectral image data of the soybean field for the years 2017-2023 were obtained from the Planet Scope satellite data provider. This satellite-based remote sensing technology was employed to detect and map plant stress induced by saline soil in the study area. The selection of Planet as a data provider was influenced by its ability to offer free data with a spatial resolution of up to 3 meters, as high-resolution data was essential due to the small size of the selected soybean field. While other remote sensors, such as Landsat and Sentinel-2, also provide valuable free data and can effectively represent patterns in the field, this thesis focused on Planet and drone data due to their higher resolution. Given that the study area is a small agricultural field, the higher resolution of these sensors was essential for capturing the finer details necessary for this research. The comparison result of the NDVI maps generated from Sentinel and Planet data highlights the significant impact of the spatial resolution of these sensors on monitoring vegetation stress caused by soil salinization, particularly in small fields.

Colour composites and NDVI index computations were performed using multispectral image data to detect plant stress caused by soil salinity. Various colour composites are known to be effective in assessing vegetation health and density. Due to the absence of shortwave infrared bands in the multispectral imagery data provided by Planet Scope, colour composite studies were limited to the Red, Red_{edge}, Green, and NIR bands. Nonetheless, the colour composites prepared using NIR-Red-Green and NIR-Red_{edge}-Green band combinations yielded valuable insights into the vegetation health and density of the soybean field.

The colour composite maps created for the years 2017-2023 provided a chronological representation of the vegetation density and health of the study area over a span of seven years. Notably, in the vicinity of sampling point 4, the lack of red colour tones, indicative of healthy and dense vegetation, points to vegetation stress in this part of the field. It is important to recall that the highest salinity values recorded in laboratory analyses were from the extract prepared with the sample taken from sampling point 4, providing evidence of consistency between the results of the two studies. The NDVI maps and soil salinity determinations suggest the existence of a preferential direction of infiltration from the river in the area around this point.

NDVI index computation studies were also conducted over a period of seven years. Upon interpreting the maps generated from these NDVI computations, it is observed that the NDVI values in the areas surrounding sampling points 3 and 4 range between 0.5 and 0.6. Since it is established that these NDVI values correspond to vegetation of medium health and sparse density, it further confirms that the soybean field is affected by soil salinity, leading to stress in the vegetation.

Given that the soybean field covers a small area, and acknowledging the importance of high-resolution imagery, even though Planet Scope data was utilized due to its high resolution, drone-based technology was additionally employed to acquire even higher-resolution multispectral images, providing finer detail in specific areas of the study. The multispectral data collected via drone were processed using MetaShape software, resulting in the generation of an orthomosaic map. This map was subsequently used in mapping studies, including NDVI

index computations and natural colour composite presentations for salinity detection in the soybean field. The use of 2D models significantly enhances our ability to visualize and analyse spatial data, leading to more informed decision-making in agricultural management and soil salinity mitigation.

The effectiveness in detecting salinity-affected lands using drone technology is influenced by the maturity of the vegetation cover in the agricultural area. The multispectral images obtained by drone during the second week of July were not suitable for the related study, as the soybean crops had not yet matured, making it challenging to identify the immature vegetation on the generated orthomosaic map. A second drone acquisition was performed on 29 August, with soybean plants at full maturity and the data are being processed.

By employing satellite and drone-based remote sensing technologies, complemented by laboratory data, the impact of saline soil on vegetation stress was identified for a soybean field in the Po River Delta through mapping studies utilizing the NDVI index. In previous salinity detection and mapping studies, the combination of field, laboratory, and remote sensing technologies has not been frequently utilized, and mapping efforts with satellite-based remote sensing sensors have often lacked support from drone-based remote sensing devices. This thesis demonstrates that by integrating various methods, the limitations inherent in each method can be mitigated by the strengths of another, thereby enhancing the reliability of saline soil detection studies in agricultural lands.

It is recommended that future research combining different methods for detecting salinity-affected agricultural lands would be beneficial in confirming the accuracy of the results. Furthermore, the use of drone-based remote sensing devices, which can provide high-resolution data for imaging studies of small areas, should be encouraged, especially for researchers operating with limited budgets, as these methods can be incorporated into their studies at a low cost.

CHAPTER 6: CONCLUSION

This study aimed to investigate the characterization of salinity-affected agricultural areas in the Po River Delta, focusing on the impact of soil salinity on vegetation stress in a selected soybean field. Through a combination of in situ observations, laboratory analyses, and advanced remote sensing techniques, including both satellite and drone-based imaging, this research provided a comprehensive assessment of salinity's effects on agricultural productivity.

The findings revealed that soil salinity levels within the soybean field exhibited significant variability, with the highest electrical conductivity values identified at sampling points in the center of the field. These measurements confirmed the presence of strongly saline soils, which are known to adversely affect crop health. NDVI computations further illustrated the negative impact of soil salinity on vegetation, with values indicating medium-low health and sparse density, particularly in the areas surrounding the most saline sampling points.

The integration of drone technology proved to be a vital component of this research, enabling the acquisition of high-resolution multispectral images that enhanced the understanding of vegetation stress. The generation of an orthomosaic map facilitated the detection of salinity impacts on the soybean field, highlighting the importance of vegetation maturity in remote sensing applications. By employing both satellite and drone-based methods, this study demonstrated that the combination of different technologies can yield complementary insights, thereby increasing the reliability and accuracy of salinity detection in agricultural contexts.

The innovative approach adopted in this thesis underscores the value of integrating multiple methodologies, as it allows for a more nuanced understanding of the challenges posed by soil salinity. Moreover, it highlights the potential for drone-based remote sensing to serve as an accessible and cost-effective tool for researchers facing budgetary constraints, particularly in studies of small agricultural areas.

In conclusion, this research contributes to the growing body of knowledge on salinity-affected agricultural lands and provides a framework for future studies to build upon. The findings emphasize the importance of monitoring soil salinity and its impact on crop health, which is critical for developing sustainable agricultural practices in regions vulnerable to salinization. Future research should continue to explore the synergies between various remote sensing technologies and field-based assessments, ultimately advancing our understanding of soil salinity dynamics and supporting effective management strategies in agricultural landscapes.

REFERENCES

1 Abbas, A., and Khan, S. (2007). Using remote sensing techniques for appraisal of irrigated soil salinity. MODSIM07 - Land, Water and Environmental Management: Integrated Systems for Sustainability, Proceedings, no. January 2007. pp. 2632–2638

2 Abdelfattah, M. A., Shahid, S. A., Othman, Y. (2008). A model for salinity mapping using Remote Sensing and GeographicInformation Systems – A Case Study from Abu Dhabi Emirate, UAE

3 Abdusamea, R. M. (2018), The Importance of the Normalized Difference Vegetation Index (NDVI) and the Use of the ArcGIS to create NDVI Maps. ISSN: 2312 – 4962

4 Acosta, J.A., Cano, A. F., Arocena, J. M., Debela, F., Martinez-Martinez, S. (2009). Distribution of metals in soil particle size fractions and its implication to risk assessment of playgrounds in Murcia City (Spain). Geoderma. 149:101–109. doi:10.1016/j.geoderma.2008.11.034

5 Ahmed, M., Toth; Z., and Decsi, K. (2024). The Impact of Salinity on Crop Yields and the Confrontational Behavior of Transcriptional Regulators, Nanoparticles, and Antioxidant Defensive Mechanisms under Stressful Conditions: A Review. International Journal of Molecular Sciences 25, 2654.

6 Allbed, A., and Kumar, L. (2013). Soil salinity mapping and monitoring in arid and semi-arid regions using remote sensing technology: A review. Advances in Remote Sensing, 2(4), 373-385. DOI: 10.4236/ars.2013.24040

7 Allbed, A., Kumar, L. (2013), Soil Salinity Mapping and Monitoring in Arid and Semi-Arid Regions Using Remote Sensing Technology: A Review. Adv. Remote Sens., 2, 404–420

8 Al-Rajahi, A., Al-Shayeb, S. M., Seaward, M. R. D., Edwardst, H. G. M. (1996). Particle size effect for metal pollution analysis of atmospherically deposited dust. Atmos. Environ. 30:145–153

9 Apollo Mapping, PlanetScope Satellite, 2024
https://docs.sentinelhub.com/api/latest/data/planet/planetscope/#:~:text=PlanetScope%20is%20one%20of%20the,subscription%3A%20Sandbox%20Data%20for%20PlanetScope.

10 Atta, M. S., Shahid, S. A., Hussain, M., and Rizvi, H. (2023). Impact of Soil Salinity on Plant Growth and Crop Yield: A Comprehensive Review. Agricultural Water Management, 275, 107875. DOI: 10.1016/j.agwat.2023.107875

11 Bannari, A. A., Abderrahmane, E., El Harti, A. (2008). Characterization of Slightly and Moderately Saline and Sodic Soils in Irrigated Agricultural Land using Simulated Data of Advanced Land Imaging (EO-1) Sensor, Communications In Soil Science and Plant Analysis. doi: 10.1080/00103620802432717

12 Bastiaanssen, W. G. M., Molden, D. J., and Makin, I. W. (2000). Remote sensing for irrigated agriculture: Examples from research and possible applications. Agricultural Water Management. DOI: 10.1016/S0378-3774(99)00035-7

13 Brouwer, C. Goffeau, A., and Heibloem, M. (1985). Irrigation Water Management: Training Manual No. 1 - Introduction to Irrigation, Chapter 7-Salt Soils, FAO - Food and Agriculture Organization of the United Nations

14 Brown, J.W., Hayward, H.E., Richards, A., Bernstein, L., Hatcher, J.T., Reeve, R.C., Richards, L.A. (1954). Diagnosis and improvement of saline and alkali soils. United States Department of Agriculture, Agriculture Handbook.

15 Chen, X.H., Duan, Z. H., Luo, T.F. (2014). Changes in soil quality in the critical area of desertification surrounding the Ejina Oasis, Northern China. Environ Earth Sci.: 72:2643–2654. doi:10.1007/s12665-014-3171-3

16 Dalton, F. N., Rhoades, J. D., and Sorrells, A. D. (1984). Soil water content and salinity measurements using time domain reflectometry. Soil Science Society of America Journal, 48(2), 334-337. DOI: 10.2136/sssaj1984.03615995004800020029x

17 De Dapper, M., Goossens R., van Ranst, E. (1997). Soil salinity and waterlogging in the Ismailia Governorate, Egypt. Telsat III/13 project. Belgium Egypt Scientific Collaboration.

18 Dehaan, R. L., Taylor, G. R. (2002). Field-derived spectra of salinized soils and vegetation as indicators of irrigation-induced soil salinization, International Journal of Remote Sensing 80:406–417

19 Dehaan, R., and Taylor, G. R. (2003). Field-derived spectra of salinized soils and vegetation as indicators of irrigation-induced soil salinization. Remote Sensing of Environment. DOI: 10.1016/S0034-4257(03)00126-4

20 Douaoui, A. E .K., Nicolas, H., Walter, C. (2006). Soil and remote-sensing data detecting salinity hazards within a semiarid context by means of combining soil and remote-sensing data, no. August 2018. Geoderma, 134(1–2):217–230. DOI: 10.1016/j.geoderma.2005.10.009

21 Flowers, T. J., and Yeo, A. R. (1995). Breeding for salinity resistance in crop plants: Where next? Food Production, 47(2), 5-14. DOI: 10.1016/0167-8809(94)00009-B

22 Gad, M. M. El-Sayed, Mohamed, M. H. A., Mohamed, M. R. (2022). Soil salinity mapping using remote sensing and GIS. Canadian Science Publishing Research article, 295

23 Gandhi, G. M., Parthiban, S., Thummalu, N., Christy, A. (2015), NDVI: Vegetation change detection using remote sensing and GIS - A case study of Vellore District. 3rd International Conference on Recent Trends in Computing, Procedia Computer Science, 57: 1199 – 1210

24 George, R. J., McFarlane, D. J., & Nulsen, R. A. (2012). Salinity in Australia: Its extent, prognosis, and research needs. Australian Journal of Soil Research, 35(5), 123-131.

25 Ghassemi, F., Jakeman, A. J., and Nix, H. A. (1995). Salinisation of land and water resources: Human causes, management, and case studies. UNESCO.
https://doi.org/10.3390/ijms25052654

26 Gibbs, S. (2000). Salinity notes: How to texture soils & test for salinity, Number 8, ISSN 1 325-4448

27 Gitelson, A., Merzlyak, M. N. (1994), Spectral reflectance changes associated with autumn senescence of Aesculus hippocastanum L. and Acer platanoides L. leaves. Spectral features and relation to chlorophyll estimation, J. Plant Physiol., vol. 143, no. 3, pp. 286–292

28 Guerra-Chanis, G. E., Reyes-Merlo, M. A., Díez-Minguito, M., Valle-Levinson, A. (2019). Saltwater intrusion in a subtropical estuary. Estuarine, Coastal and Shelf Science, 217, 28e36.

29 Guo, B., Han, B., Yang, F., Fan, Y., Jiang, L., Chen, S., Yang, W., Gong, R., Liang, T. (2019), Salinization Information Extraction Model Based on VI–SI Feature Space Combinations in the Yellow River Delta Based on Landsat 8 OLI Image. Geomat. Nat. Haz. Risk, 10, 1863–1878.

30 Hardie, M., Doyle, R. B. (2012). Measuring Soil Salinity, Methods in molecular biology (Clifton, N.J.). doi: 10.1007/978-1-61779-986-0_28

31 Khan, M. A., and Duke, N. C. (2018). Seawater Intrusion Impacts on Coastal Agriculture. Journal of Coastal Research, 34(4), 902-913.

32 Khan, N. I., Mohiuddin, M., and Zhang, Y. (2005). Remote sensing techniques to assess waterlogging and salinity conditions of agricultural land: A case study from the Punjab Province, Pakistan. Journal of Arid Environments. DOI: 10.1016/j.jaridenv.2005.03.014

33 Khan, N. M., Rastoskuev, V. V., Shalina, E. V., and Sato, Y. (2001). Mapping salt-affected soils using remote sensing indicators-a simple approach with the use of GIS IDRISI. 22nd Asian Conference on Remote Sensing, 5(9). Major, D., Baret, F., and Guyot, G. 1990. A ratio vegetation index adjusted for soil brightness. Int. J. Remote Sens. 11:727 740. doi:10.1080/01431169008955053

34 Li, Z., and Yang, Y. (2018). Remote Sensing Techniques for Monitoring Land Degradation and Desertification. Remote Sensing. DOI: 10.3390/rs10040558

35 Ljung, K., Selinus, O., Otabbong, E., Berglund, M. (2006). Metal and arsenic distribution in soil particle sizes relevant to soil ingestion by children, Appl. Geochem. 21:1613–1624. doi:10.1016/j. apgeochem.2006.05.005

36 Luo, J., Straffelini, E., Bozzolan, M., Zheng, Z., Tarolli, P. (2023). Saltwater intrusion in the Po River Delta (Italy) during drought conditions: Analyzing its spatio-temporal evolution and potential impact on agriculture, International Soil and Water Conservation Research. 12(2024)714-725

37 Major, D., Baret, F., and Guyot, G. (1990). A ratio vegetation index adjusted for soil brightness. Int. J. Remote Sens. 11:727–740. DOI:10.1080/01431169008955053.

38 McNeill, J. D. (1980). Electromagnetic methods for soil conductivity measurements. Geonics Limited Technical Note TN-6. DOI: Not applicable; Technical Note from Geonics Limited.

39 Metternicht, G., and Zinck, J. A. (2003). Remote sensing of soil salinity: Potentials and constraints. Remote Sensing of Environment. DOI: 10.1016/S0034-4257(02)00188-8

40 Morshed, M.M., Islam, M.T., and Jamil, R. (2016). Soil salinity detection from satellite image analysis: an integrated approach of salinity indices and field data. Environ. Monit. Assess. 188: 119. doi: 10.1007/s10661-015-5045-x. PMID: 26815557.

41 Mulla, D. J. (2013). Twenty-five years of remote sensing in precision agriculture: Key advances and remaining knowledge gaps. Biosystems Engineering. doi: 10.1016/j.biosystemseng.2012.08.009

42 Munns, R., & Tester, M. (2008). Mechanisms of salinity tolerance. Annual Review of Plant Biology, 59(1), 651-681.

43 Nawar, S., Buddenbaum H., Hill, J. (2015). Estimation of soil salinity using three quantitative methods based on visible and near-infrared reflectance spectroscopy: a case study from Egypt. Arab. J. Geosci. 8:5127–5140. doi:10.1007/s12517-014-1580-y

44 Oosterbaan, R. J. (2020). Soil salinity, Conference paper, pp. 1.

45 Peralta, N. R., and Costa, J. L. (2013). Delineation of management zones with soil apparent electrical conductivity to improve nutrient management. Computers and Electronics in Agriculture. DOI: 10.1016/j.compag.2013.03.006

46 Peterson, F. (2001). Coastal Salinity Intrusion. In M. N. Shende (Ed.), Water Quality in the Coastal Zone (pp. 27-39). Academic Press.

47 Qadir, M., Ghafoor, A., and Murtaza, G. (2007). Use of saline-sodic waters through phytoremediation of calcareous saline-sodic soils. Agricultural Water Management, 50(3), 197-210.

48 Rao, B. R. M., and Dekker, A. G. (2014). Remote sensing of coastal and inland waters: A review. Remote Sensing. DOI: 10.3390/rs60612723

49 Rayment, G. E., Higginson, F. R. (1992). Australian laboratory handbook of soil and water chemical methods. Inkata Press, Melbourne

50 Rengasamy, P. (2006). World salinization with emphasis on Australia. Journal of Experimental Botany, 57(5), 1017-1023

51 Rhoades, J. D., Chanduvi, F., Lesch, S. (1999). Soil salinity assessment, Methods and interpretation of electrical conductivity measurements, FAO Irrigation and Drainage paper 57. ISSN0254-5284

52 Rouse, Jr. J., Haas, R., Schell, J., Deering, D. (1974), Monitoring vegetation systems in the great plains with ERTS, NASA, Washington, DC, USA, vol. 351, pp. 309–317

53 Sahbeni, G., Ngabire, M., Musyimi, P. K., Székely, B. (2023), Challenges and Opportunities in Remote Sensing for Soil Salinization Mapping and Monitoring: A Review. Remote Sens., 15, 2540 https://doi.org/10.3390/rs15102540

54 Samouëlian, A., Ghrabi, A., and Cousin, I. (2005). Soil water content and salinity measurements with resistivity sensors: Principles and applications. Geoderma, 124(1-2), 81-96. DOI: 10.1016/j.geoderma.2004.04.003

55 Sentinel Hub, PlanetScope, 2024 https://docs.sentinelhub.com/api/latest/data/planet/planetscope/#:~:text=PlanetScope%20is%20one%20of%20the,subscription%3A%20Sandbox%20Data%20for%20PlanetScope.

56 Shrestha, R. K., and Farshad, A. (2009). Mapping salinity and waterlogging hazards in Iran: Application of different techniques and methods. The World Bank

57 Shrivastava, P., and Kumar, R. (2015). Soil salinity: A serious environmental issue and plant growth promoting bacteria as one of the tools for its alleviation. Saudi Journal of Biological Sciences, 22(2), 123-131

58 Sudduth, K. A., Kitchen, N. R., and Wiebold, W. J. (2005). Remote sensing for precision agriculture: The role of optical sensors. Journal of Precision Agriculture, 6(1), 17-32. DOI: 10.1007/s11119-005-1823-6

59 Tarolli P, Luo J, Straffelini E, Liou Y-A, Nguyen K-A, Laurenti R, Masin, R., and D'Agostino, V (2023). Saltwater intrusion and climate change impact on coastal agriculture. PLOS Water 2(4): e0000121
https://doi.org/10.1371/journal.pwat.0000121

60 USGS, NDVI, the Foundation for Remote Sensing Phenology, 2024
https://www.usgs.gov/special-topics/remote-sensing-phenology/science/ndvi-foundation-remotesensingphenology#:~:text=Although%20there%20are%20several%20vegetation,from%20%2B1.0%20to%20%2D1.0.

61 Verma, R. K., Pal, P. K., and Das, P. K. (1994). Satellite remote sensing of soil salinity in the Great Rann of Kachchh, Gujarat, India. International Journal of Remote Sensing. DOI: 10.1080/01431169408954161

62 Watson, M. (2005). Natural Sources of Soil Salinity. Agriculture and Environment Journal, 12(2), 45-57.

63 Weather Spark, Climate and Average Weather Year Round in Porto Tolle - Italy, 2024
https://weatherspark.com/y/72350/Average-Weather-in-Porto-Tolle-Italy-Year-Round

64 Xie, Q., Huang, W., Peng, D., Casa, R. (2018). Vegetation Indices Combining the Red and Red-Edge Spectral Information for Leaf Area Index Retrieval. Article in IEEE Journal of Selected Topics in Applied Earth Observations and Remote Sensing. doi: 10.1109/JSTARS.2018.2813281

65 Yadav, R. L., and Singh, S. K. (2015). Soil Salinity: Historical Perspectives and the Contribution of Civilizations in Developing Saline Soils. In M. L. Aggarwal (Ed.), Soil Salinity Management in Agriculture (pp. 3-22). DOI: 10.4067/S0718-95162015000100003

66 Zhang, C., and Kovacs, J. M. (2012). The application of small unmanned aerial systems for precision agriculture: a review. Precision Agriculture. DOI: 10.1007/s11119-012-9253-7

67 Zhao, Y., Feng. Q., Yang, H. (2016). Soil salinity distribution and its relationship with soil particle size in the lower reaches of Heihe River, North-western China, Environ Earth Sci. doi: 10.1007/s12665-016-5603-8

68 Zhu, L., Suomalainen, J., Liu, J., Hyyppä, J., Kaartinen, H., Haggren, H. (2017), A Review: Remote Sensing Sensors, Multi-Purposeful Application of Geospatial Data; IntechOpen: London, UK

69 Zinck, J. A. (2001). Monitoring salinity from remote sensing data. In R. Goossens & B. M. De Vliegher (Eds.), Proceeding of the 1st Workshop of the EARSeL Special Interest Group on Remote Sensing for Development Countries (pp. 359-368). Belgium: Ghent University.

70 Zribi, M., Baghdadi, N., Lili-Chabaane, Z., Loumagne, C., Baup, F., Ben Slimane, A., and Cheviron, B. (2011). Soil surface moisture estimation over a semi-arid region using ENVISAT ASAR radar data for several incidence angles and polarization modes. Remote Sensing of Environment. DOI: 10.1016/j.rse.2011.06.02

APPENDIX

Table A1

Instruments and devices used in laboratory procedures.

Instrument	Conductometer (WTW-Cond 340i)	Deionized water	Orbital shaker	Cool oven (Memmert)	Precision scale	Plastic bag
Image					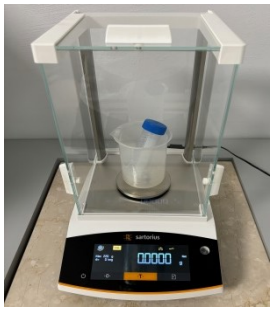	
Instrument	Plastic beaker	Plastic tube	Mortar and pestle	Rolling pin	Plastic spoon spatulas	Sieve (2 mm)
Image